Dynamic Rupture Propagation on Fault Planes with Explicit Representation of Short Branches

Authors' information:
Xiao Ma: xiaoma5@illinois.edu, Ahmed E. Elbanna: elbanna2@illinois.edu
Department of Civil and Environmental Engineering, University of Illinois at Urbana-Champaign, Illinois, US

Dynamic Rupture Propagation on Fault Planes with Explicit Representation of Short Branches

Xiao Ma *[1] and Ahmed Elbanna[1]

[1]Department of Civil and Environmental Engineering, University of Illinois, Urbana-Champaign, Illinois, USA

Abstract

An active fault zone is home to a plethora of complex structural and geometric features that are expected to affect earthquake rupture nucleation, propagation, and arrest, as well as interseismic deformation. Simulations of these complexities have been largely done using continuum plasticity or scalar damage theories. In this paper, we use a highly efficient novel hybrid finite element-spectral boundary integral equation scheme to investigate the dynamics of fault zones with small scale pre-existing branches as a first step towards explicit representation of anisotropic damage features in fault zones. The hybrid computational scheme enables exact near-field truncation of the elastodynamic field allowing us to use high resolution finite element discretization in a narrow region surrounding the fault zone that encompasses the small scale branches while remaining computationally efficient. Our results suggest that the small scale branches may influence the rupture in ways that may not be realizable in homogenized continuum models. Specifically, we show that these short secondary branches significantly affect the post event stress state on the main fault leading to strong heterogeneities in both normal and shear stresses and also contribute to the enhanced generation of high frequency radiation. The secondary branches also affect off-fault plastic strain distribution and suggest that co-seismic inelasticity is sensitive to pre-existing damage features. We discuss our results in the larger context of the need for modeling earthquake ruptures with high resolution fault zone physics.

*xiaoma5@illinois.edu

1 Introduction

The internal structure of fault zones in the upper continental crust exhibits considerable complexity. There is variation along strike in the form of bends and segmentation, and with depth due to changes in deformation mechanism, including brittle to ductile transition. Mature faults consist of several basic structural elements including: (i) A zone of concentrated shear, the fault core, which is often defined by the presence of extremely comminuted gouge; (ii) A damage zone, with the primary fault core centralized in or bordering that damage zone, in addition to a segmented network of several secondary cores within the damage zone. Damage zones display a greater intensity of deformation relative to the surrounding host rock, and contain features such as secondary faults and fractures, microfractures, folded strata, and comminuted grains; and (iii) host country rock with little or no damage. In general, the intensity of damage increases towards the fault core and the transition from undeformed host rock to damage zone rock is often gradual [Chester et al.1993, Ben-Zion and Sammis2003, Savage and Brodsky2011]. Overall, fault zones exhibit a combination of distributed damage as well as discrete anisotropic secondary fractures of different orientations and density [Rowe et al.2018].

Off-fault damage has been investigated extensively using numerical models that implement either off-fault plastic strain accumulation [Andrews2005, Templeton and Rice2008, Hok et al.2010, Dunham et al.2011a, Dunham et al.2011b], or continuum damage evolution [Ben-Zion and Shi2005, Xu et al.2015a, Bhat et al.2012]. The starting point in both approaches is a virgin material that has not experienced damage before. Furthermore, both approaches are found to be prone to numerical localization and have been, for the large part, constrained to scalar damage variables or isotropic formulations [Duru and Dunham2016, Uphoff et al.2017]. Except for a few pioneering studies, for example [Dunham et al.2011b, Shi and Day2013, Tal et al.2018], that considered off-fault dissipation generated by rough fault surfaces, most of the prior studies considered planar faults with no structural complexity. In particular, the effect of pre-existing anisotropic damage features on rupture dynamics, in both the elastic and inelastic regimes, remains an area that is under-studied.

An exception to the aforementioned discussion has been the investigation of the critical problem of the influence of a fault branch on the termination or continued propagation of rupture on the main fault [Poliakov et al.2002, Kame et al.2003, Bhat et al.2004, Biegel et al.2007, Rousseau and Rosakis2009, Suzuki2013]. These studies suggest that the rupture may continue to propagate on the main fault without jumping to the branch, or propagate on both the main and secondary faults, or terminate on the main fault and continue on the branch. The fate of the rupture depends on the angle of the branch, the background stress field, and the rupture propagation speed.

However, to the best of our knowledge, all these studies have been limited to a single long branch. Short and repeated branches that are routinely mapped in fault zones [Rempe et al.2013, Rowe et al.2018] are largely neglected or homogenized as an effective damage variable. An outstanding challenge in explicit modeling of these anisotropic secondary features has been largely attributed to the prohibitive computational cost in terms of problem size, runtime, and memory requirements of domain-based methods such as finite element or finite difference techniques.

Domain based modeling approaches are very versatile in handing complex geometries and material nonlinearities compared to boundary-based methods such as the spectral boundary integral equation. However, to capture small scale details associated with short fault branches, a very fine mesh must be used to resolve the complex boundaries as well as the multiple stress concentration regions associated with the propagating rupture tips. This fine mesh is generally carried out for a significant portion of the domain to appropriately propagate the seismic waves and avoid artificial reflection from varying the mesh size over small distances. Furthermore, the simulation domain has to be truncated at some distance by imposing absorbing boundary conditions [Lysmer and Kuhlemeyer1969, Bettess1977, Berenger1994] far enough from the fault so that reflections from these boundaries do not affect the solution on the fault plane during the simulation time of interest. As a result, the computation cost of a domain-based method grows as $(L/dx)^3$ in 2D and $(L/dx)^4$ in 3D, making it very challenging to incorporate small scale physics in large scale simulations.

A novel approach in addressing the above challenge has been recently presented by [Klinger et al.2018], who combined optical image correlation, field observation, and a new numerical method for dynamic rupture simulations using discrete finite element model to study co-seismic off-fault damage generation resolving complex rupture process. The numerical method presented by Klinger et al. enabled generation of co-seismic damage patterns that localize into a set of nearly periodic parallel branches. While their formulation is based on continuum damage theory, the damage parameter may numerically localize and eventually be replaced by a slip-weakening crack. Earlier work by [Ando and Yamashita2007] has also provided a framework for spontaneous generation of off-plane faults using a novel formulation of the boundary integral method. However, what continues to be missing in this work is the effect of pre-existing secondary cracks, which is expected to influence the dynamic rupture characteristics high frequency radiation and new damage generation, in a way that is different from co-seismically generated damage in a virgin material. In this paper we plan to address this missing piece using a novel numerical scheme that enables incorporating high resolution fault zone physics and geometric structures in dynamic rupture calculations.

Here, we use our recently developed hybrid computational scheme that combines a domain-based numerical method which is used to discretize a confined region encompassing the fault plane and all its related structural and material complexities, with an independent spectral boundary integral formulation that models the exterior linear elastic half spaces [Hajarolasvadi and Elbanna2017, Ma et al.2018]. This approach overcomes the limitations of the domain-based methods by limiting the discretization to only a subset of the whole domain but benefits from their flexibility in modeling complex geometry and material nonlinearity. The reduction in the size of the domain to be discretized enables us to use higher resolution within the fault zone to resolve the complexity of the secondary branches while saving computational cost and not compromising the accuracy of long range elastodynamic interactions, which are handled exactly using the spectral boundary integrals. In our prior work [Ma et al.2018] we have discussed the novelty of our hybrid formulation in the context of existing literature on coupling boundary and bulk numerical schemes as in [Bielak et al.2003, Yoshimura et al.2003]. In this paper, we will use the hybrid scheme to investigate the dynamics of rupture propagation on a fault plane with multiple short branches mimicking the fish bone architecture idealized in [Sowers et al.1911, Poliakov et al.2002].

The remainder of the paper is organized as follows. In Section 2, we describe the model setup and give an overview of the hybrid numerical scheme. In Section 3, we summarize the numerical simulation results from explicitly modeling the fault zone complexity. In Section 4, we discuss the new insights from the consideration of the anisotropic and discrete damage features that exist in complex fault zones. In Section 5, we summarize our conclusions.

2 Numerical method and model Setup

2.1 Hybrid Finite Element-Spectral Integral Equation Method

We solve the initial boundary value problem of dynamic fracture using the recently developed hybrid method [Ma et al.2018]. The hybrid method is a combination of the FEM (finite element method) and SBI (spectral boundary integral method), although any other domain-based method may be used in lieu of FEM. In the hybrid method, all nonlinearities, such as fault surface roughness or material nonlinearity, as well as small-scale heterogeneities, are contained in a virtual strip of a certain width that is introduced for computational purposes only (Fig. 1). Appropriate meshing techniques are then used to discretize and model this strip using FEM. The step-by-step time integration approach for the fault nodes is a central-difference explicit formulation as follows:

$$\dot{u}^{n+1/2} = \dot{u}^{n-1/2} + \Delta t\, M^{-1}(T^n - f^n) \tag{1}$$

$$u^{n+1} = u^n + \Delta t\, \dot{u}^{n+1/2} \tag{2}$$

where $\dot{}$ represents the partial derivative with respect to time and the superscript n indicates the time step index. M is the lumped mass matrix. T_n is the traction on the fault interface based on the fault discontinuity condition. The fault discontinuity condition is implemented using the Traction at Split Nodes (TSN) method [Day1982]. f is the internal force due to the deformation of the solid and Δt the time step.

For the interior nodes in the FEM domain, the step-by-step time integration approach is as follows:

$$\dot{u}^{n+1/2} = \dot{u}^{n-1/2} + \Delta t\, M^{-1}(-f^n) \tag{3}$$

$$u^{n+1} = u^n + \Delta t\, \dot{u}^{n+1/2} \tag{4}$$

The rest of the domain, which is homogeneous and linear-elastic, may be modeled as two half spaces coupled with this strip on each side (S^+, S^-). The elastodynamic response of these half spaces is modeled using the SBI technique. Throughout the simulation, the two methods communicate along the virtual boundaries of the strip by exchanging displacement and traction boundary conditions. The spectral formulation for this method gives an exact form of such a relationship in the Fourier domain. We use the spectral formulation introduced in [Geubelle1995], where the elastodynamic analysis of each half space is carried out separately. In view of the hybrid method, where SBI constitutes a boundary condition to the FEM model, we focus the description on modeling a half-space. The relationship between the traction τ_i and the resulting displacements at the boundary of a half-space may be expressed as

$$\begin{aligned} \tau_1^{\pm}(x_1,t) &= \tau_1^{0\pm}(x_1,t) \mp \frac{\mu}{c_s}\dot{u}_1^{\pm}(x_1,t) + f_1^{\pm}(x_1,t) \\ \tau_2^{\pm}(x_1,t) &= \tau_2^{0\pm}(x_1,t) \mp \frac{(\lambda+2\mu)}{c_p}\dot{u}_2^{\pm}(x_1,t) + f_2^{\pm}(x_1,t) \end{aligned} \tag{5}$$

where subscripts 1 and 2 represent fault-parallel and fault-normal direction respectively, $\pm$ represents upper and lower half-plane, c_p is the pressure wave speed, c_s is the shear wave speed, τ_i^0 indicates the externally applied load (*i.e.*, at infinity); and f_i are linear functionals of the prior deformation history and are computed by the time convolution in the Fourier domain.

The coupling of the two methods is done as follows. The FEM and SBI share nodes at the virtual boundaries introduced to truncate the FEM domain. While FEM provides SBI with the tractions along the virtual boundary, SBI returns the displacement that is to be imposed on $S^{\pm}$ of FEM. The detailed step-by-step procedure is as follows

1. Solve full time step within the FEM by solving Eq. (1 - 2) (FEM interior nodes only).
2. Set interface tractions in the SBI equal to the internal force from FEM: $\tau_i^{n,\mathrm{SBI}} = f_i^{n,\mathrm{FEM}}$, where f_i^n is given through Eq. 1.
3. Solve full time step within SBI by solving Eq. (5) for velocity and apply explicit integration scheme to get displacements.
4. Set displacements of the shared nodes in FEM equal to displacement in SBI: $u_i^{n+1,\mathrm{FEM}} = u_i^{n+1,\mathrm{SBI}}$.
5. Return to Step 1 to advance to the next time step.

For a full description of the hybrid scheme, its verification, and some of its prior applications please refer to [Ma et al.2018].

2.2 Model Setup

2.2.1 Material and Friction model

In this paper, we consider both linear elastic material and elasto-plastic material.

Linear elastic Material

A 2D plane strain elastic model is used to describe the elastic material behavior. The constitutive equation for the linear elastic material is as follows:

$$\sigma_{ij} = \lambda \delta_{ij} \varepsilon_{kk} + 2\mu \varepsilon_{ij} \tag{6}$$

where ε_{ij} is the infinitesimal strain tensor and μ, λ are the Lamé parameters.

Elasto-Plastic Material

In this paper, we also consider the off-fault material to be idealized with the Drucker-Prager plasticity model [Drucker and Prager1952]. The Drucker-Prager model is closely related to the

Mohr-Coulomb model. It describes inelastic deformation in brittle solids arising from frictional sliding of microcracks [Rudnicki and Rice1975, Templeton and Rice2008]. We use the Drucker-Prager plasticity model to mimic the inelastic effects on dynamic rupture from cracks on scales that are smaller than the scale of branches. The yield function of the Drucker-Prager plasticity model is given by Eq.7,

$$F(\sigma_{ij}) = \sqrt{J_2} - (A + BI_1) \tag{7}$$

Here, $I_1 = \sigma_{kk}$ is the first invariant of the Cauchy stress σ_{ij} and $J_2 = s_{ij}s_{ij}/2$ is the second invariant of the deviatoric stress tensor $s_{ij} = \sigma_{ij} - (\sigma_{kk}/3)\delta_{ij}$. Following [Templeton and Rice2008], we take the intermediate principal stress, in the Drucker-Prager formulation, to be the average of the maximum and the minimum principle stress. The constants A and B are determined from experiments and are functions of the cohesion c and the angle of internal friction ϕ that are used to describe the Morh-Coulomb yield surface. When $F(\sigma_{ij}) < 0$, the material response is elastic. Plastic flow is partitioned between various components of the plastic strain rate tensor by the flow rule. Neglecting the effect of plastic dilatancy we have:

$$\dot{\epsilon}^p_{ij} = \dot{\epsilon}^{eq}_p s_{ij}/(2\sqrt{J_2}) \tag{8}$$

Where $\dot{\epsilon}^{eq}_p = \sqrt{2\dot{\epsilon}^p_{ij}\dot{\epsilon}^p_{ij}}$ is the equivalent plastic strain rate. The equivalent plastic strain ϵ^{eq}_p is defined through $\dot{\epsilon}^{eq}_p = d\epsilon^{eq}_p/dt$

Slip-weakening friction model

In this paper, all the faults are governed by the slip-weakening friction law [Ida1972]. The frictional strength is given by

$$f(D) = \begin{cases} f_s - (f_s - f_d)D/D_c, & D < D_c \\ f_d, & D \geq D_c \end{cases} \tag{9}$$

where f_s and f_d are the static and dynamic frictional coefficients and D_c the critical slip required for stress to reach the dynamic value. Continuity of displacements at the fault is enforced (*i.e.*, no slip) if the shear traction is lower than frictional strength, otherwise local slip occurs. Uenishi and Rice [Uenishi and Rice2003] defined the characteristic length scale for frictional instability on linear slip-weakening faults. We base our reference length scale for normalizing the spatial scales in our problem on this characteristic length scale term as shown in Eq. 10 (omitting the constant term from [Uenishi and Rice2003]).

$$L_c = \frac{\mu D_c}{\tau_s - \tau_d} \tag{10}$$

Here, μ is the shear modulus, D_c is the characteristic slip distance, τ_s is the static frictional stress and τ_d is the dynamic frictional stress.

Normal Stress Regularization

Due to the complex topology of our fault network, normal stress may be altered on the main fault as well as secondary faults. In order to avoid numerical instability and for the friction model to be compatible with laboratory observations, we include normal stress regularization following priors studies [DeDontney et al.2012, Xu et al.2015b].

$$\frac{d\tau}{dt} = -\frac{1}{t^*}(\tau - f\sigma_N) \tag{11}$$

where the shear strength τ evolves over a finite time scale (t^*). t^* was taken to be $2\Delta x/c_s$, which is several times larger than the stable time step. Here Δx is the mesh size.

2.2.2 Geometry

We consider our fault system to exist in an infinite medium. A planar horizontal main fault is placed in the middle of the domain with secondary fault branches explicitly modeled as shown in Fig. 1. The main fault is right lateral and the secondary faults are placed on one side of the fault (on the tension side) starting at a distance L_a from the nucleation zone. This minimizes the effect of these secondary branches on the rupture nucleation. The angle between the secondary faults and main fault is assumed to be θ_f. While this angle may be arbitrary, in this paper we have explored a number of different secondary faults orientation that vary around the the direction of optimally oriented shear plane computed using the background tectonic stress field and a Mohr-Coulomb failure criterion.

$$\theta = 45^\circ + \frac{\psi}{2} - \theta_p \tag{12}$$

In Eq. 12 above, ψ is the angle of internal friction, and θ_p is the maximum principle stress direction. The secondary faults have constant spacing L_s along the fault strike. The length of each secondary fault is L_f. Vertically, the secondary fault branches are placed a small distance L_o away from the main fault. We note that other approaches may be used to handle the triple junction between the branch fault and the main fault without having to enforce this shift. This may be accomplished by manipulating the kinematics of the split nodes at the junction through either retaining the continuity of the main fault only, or the continuity of the branch fault only, or by assuming that neither fault is continuous and having only one node at the triple junction point as described in [DeDontney et al.2012]. The effect of the various modeling assumptions will be examined in future work We limit the FEM discretization to a domain of length L and width W_H. The length L is taken to be $100L_c$. The width W_H is much smaller than the length L. The domain width W_H is determined by the length of secondary branches and is taken to be $4L_c$ to ensure that the FEM domain contains the complex fault geometry. All parameters are listed in Table 1.

2.2.3 Initial and Boundary Condition

We assume the domain is in static equilibrium at time $t = 0$. We consistently resolve the normal stress σ_N and tangential stress τ on all the faults from the background stress σ_{xx}, σ_{yy} and σ_{xy} using Eq. 13 .

$$\begin{aligned} \sigma_N &= \sigma_{xx}\sin^2\theta + \sigma_{yy}\cos^2\theta - 2\tau_{xy}\sin\theta\cos\theta \\ \tau &= \sigma_{xx}\sin\theta\cos\theta - \sigma_{yy}\sin\theta\cos\theta + \tau_{xy}(\cos^2\theta - \sin^2\theta) \end{aligned} \tag{13}$$

where θ is the angle between secondary faults and the horizontal direction. We nucleate the rupture by overstressing the fault beyond the static friction strength over a localized region in its center with a width L_c. For the medium with elasto-plastic material, we apply a smooth nucleation approach. We use a union of hyperbolic tangent function to smoothly approximate an overstressing region width of L_c to avoid stress concentration from the edges of the nucleation zone. The overstressing region stress level starts at 90 percent of the fault strength and gradually increases over a period of time to reach the fault strength stress level. Other nucleation approaches could also be used such as using consistent initial slip and slip rate profile extracted from quasidynamic simulations for the nucleation process on a planar fault [Liu and Lapusta2008].

From [Andrews1976, Das and Aki1977], the relative strength parameter is defined as $S = (\tau_s - \tau)/(\tau - \tau_d)$, which quantifies the closeness of initial stress to failure relative to the stress drop. For this study, we are considering background stress conditions which correspond to strength parameter $S = 2$ on the main fault. Thus, the ambient stress conditions favor sub-Rayleigh rupture propagation on the main fault.

3 Results

To normalize our results, we adopt the following dimensionless quantities for length, time, slip, slip rate, and stress:

- Length, $x^* = x/L_c$

- Time, $t^* = tc_s/L_c$
- Slip, $D^* = D/D_c$
- Slip rate, $V^* = VL_c/(D_c c_s)$
- Stress, $\sigma^*_{ij} = \sigma_{ij}/(-\sigma^0_{yy})$

3.1 Elastic Domain

Fig. 2 compares several rupture metrics on the main fault plane with and without the short branches. The short branches lead to a reduction in the peak slip rate as well as the accumulated slip on the main fault plane. This may be explained by the fact that when the short branches are activated, the frictional slip on these secondary features contributes to the total energy dissipation leading to reduced slip and slip rate. The increased energy dissipation in the presence of the secondary branches also slows the rupture on the main fault and decreases the rupture propagation speed at least within the fish bone region. However, there is a slight increase in the slip near the center of the main fault (around $x^* = 0$) for the case with the short branches. The initiation and arrest of ruptures on the secondary branches lead to the generation of seismic signals that are reflected back on the main fault leading to ripples in the slip rate profile that propagate backward (See Video 1 from Supplementary Material) and accumulate more slip away from the rupture tip that would not have been generated in the homogeneous medium case. The reduction in slip rate and rupture speed due to increased energy dissipation has also been previously observed in models with off-fault energy dissipation using plasticity [Templeton and Rice2008] or continuum damage theories [Bhat et al.2012]. The backward propagating ripples, however, is a consequence of the geometric complexity of the model.

The secondary faults have a significant effect on the post-rupture stress distribution. Fig. 2(c) and 2(d) show that both the shear and normal stress exhibit strong spatial heterogeneities within the fish bone region after the passage of the rupture front. These strong heterogeneities are absent in the homogeneous medium case. The activation and arrest of slip on the secondary branches lead to the development of normal and shear stress concentrations at their ends which load the main fault nonuniformly. These stress fluctuations lead to both stress increase as well as reduction in both of the normal and shear stress components. In particular, the normal stress is reduced to 70% of its original value at some locations. This may suggest that some configurations of the secondary branches may even lead to fault opening, although we have not observed this yet in the cases we investigated. Furthermore, the shear stress drops to 50% of its corresponding value in the homogeneous case at several points. This is also indicative that geometric complexities may potentially lead to the reversal of the shear stress sense if they cause large enough shear stress fluctuations. This pattern of stress fluctuations on the main fault may be predicted qualitatively using Linear Elastic Fracture Mechanics (LEFM) as has been done in a previous study of dynamic rupture with a single backthrust branch fault [Xu et al.2015b]. We present an example of such calculations in Appendix A.

Another major result in this paper is the influence of secondary branches on the high-frequency generation in the bulk. Fig. 3 shows the near-field particle velocity for both cases with and without the secondary branches. For the homogeneous medium, the wave field is smooth almost everywhere with concentration of high frequencies neat the rupture tips. On the other hand, for the medium with branches, we observe coherent wave fronts that are propagating away from the tips and spaced apart periodically, consistent with the periodic distribution of the secondary branches. These coherent fronts are generated due to the constructive interference of seismic radiation from the secondary faults. We have also included videos for the process of high frequency generation in Supplementary Materials 2 and 3.

To demonstrate the enhanced generation of high frequencies for the case with the fish bone structure, we plot in Fig 4. the fault-parallel and fault-normal components of the velocity at a station located $20L_c$ from the main fault and represented by the star in Fig. 4(c). Both components of the velocity show high frequency fluctuations in the case of the fault with branches compared to the homogeneous case. The acceleration spectra plotted in Fig. 4(c) further prove this point. The fault with small branches has a spectrum that is richer in high-frequency content and furthermore shows an almost flat spectrum in the frequency range 2-20 Hz. This is consistent with observations in [Wald and Heaton1994, Chen1995] and similar to the results from dynamic rupture simulation on rough faults [Dunham et al.2011b]. This suggests that small scale fault branches may be a candidate for explaining near field radiation characteristics of active faults.

Another effect of the secondary faults is shown in Fig. 5 which illustrates the distribution of the normal displacement of the main fault plane. For the homogeneous medium, the fault plane simply rotates. The existence of the secondary branches, however, leads to the development of undulations in the fault plane profile as shown in Fig. 5. The stress concentrations corresponding to the secondary faults, load the fault in the normal direction and promote repeated peaks in its vertical profile near the locations where the secondary branches are positioned. While the magnitude of these undulations is small, they may contribute, over several cycles, to the evolution of the main fault roughness.

To gain further insight into the dynamics of the branch faults, we show in Fig. 6 the time evolution of the slip, slip rate, and the rupture speed on one of the secondary faults (the first branch). The secondary fault is triggered dynamically by the main fault rupture as it approaches the branch tip leading to a rapid increase in slip rate and slip over a segment of the branch that is closest to the main fault . As stated in Section 2, the background stress favors a sub-Rayleigh rupture propagation on the main fault. However, this is not the case for the secondary faults which are loaded dynamically from the propagating rupture on the main fault in addition to the loading from the background stress field. The insert in Fig. 6(a) shows the rupture tip position along the secondary fault versus time, and it suggests that the secondary fault fails in a supershear mode. This result suggests that even though the far field background stress favors a sub-Rayleigh rupture propagation on the main fault, the small scale branching faults may fail differently. This may potentially have important implications for seismic hazard from complex fault zones.

3.2 Elasto-Plastic Domain

To account for additional energy dissipation mechanisms at a scale smaller than the scale of the secondary branches that we haven't explicitly modeled, we consider the possibility of inelastic strain generation using an elasto-plastic material model. Since we have only considered one level of the secondary branches, the plasticity model may be used as a proxy for small scale damage that is randomly distributed and arising from microcracks or dislocation movement at nano or micro scale. Drucker-Prager plasticity is used as described in Section 2.

Figure 7 compares several rupture metrics on the main fault plane with and without the short branches but in the presence of off-fault plasticity. In this case, the rupture may generate off-fault plastic strain if the Drucker-Pragger yield criterion is met. Consistent with the elastic case, the short branches also lead to a reduction in the peak slip rate as well as the accumulated slip on the main fault plane. The frictional slip on the secondary branches contributes to the total energy dissipation leading to reduced slip, slip rate, and rupture propagation speed. However, unlike in the elastic case, there is no slight increase in the slip near the center of the main fault (around $x^* = 0$) for the case with the short branches. Plasticity, which acts as an additional energy sink on its own, has suppressed the backward propagating ripples and greatly reduced their effect. Overall, the slip, the slip rate, and the rupture speed are all lower in this case compared to the case of rupture propagation in an elastic medium.

The effect of the secondary faults on the post-rupture stress distribution persists even with plasticity. Fig. 7(c) and 7(d) show that both the shear and normal stress exhibit strong spatial heterogeneities within the fish bone region after the passage of the rupture front. These strong heterogeneities are absent in the homogeneous medium case with off-fault plasticity. The activation and arrest of slip on the secondary branches leads to the development of normal and shear stress concentrations at their ends which load the main fault nonuniformly. These stress fluctuations lead to both stress increase as well as reduction in both of the normal and shear stress components and the amplitude of the fluctuations are very similar to those generated in the elastic case indicating that they are unaffected by plasticity.

The secondary branches, as pre-existing damage features, have strong influence on the off-fault plastic strain distribution as shown in Fig. 8. While in the homogeneous case, the plastic strain distribution has the characteristic fan-like shape consistent with previous studies [Templeton and Rice2008, Dunham et al.2011a, Dunham et al.2011b], the plastic strain distribution is increasingly non-uniform due to the presence of the short branches. In particular, the spatial extent of the off-fault plasticity in the vicinity of the main fault is greatly reduced within the region that hosts the short branches. Furthermore, the short branches seem to have little or no plastic strain accumulation, suggesting that what should have been bulk plastic strain has collapsed in the form of localized slip along the short secondary fault. However, there is a large increase in the plastic strain accumulation at the ends of the short branches due to the abrupt arrest of the slip and the associated stress concentration. Namely, there is a concentration in plastic strain in the region between the secondary branch tip and the main fault suggesting that even if the branch is not directly connected to the main fault, this region will be severely damaged. Furthermore, there is another region of plastic strain concentration at the far end of the secondary fault. This region also does not extend along the strike of the secondary branches but is slightly bent in another direction suggesting a possible growth plane for the secondary faults if they are allowed to extend.

3.3 Rupture Characteristics with and without plasticity

Fig. 9(a) shows the rupture tip position versus time for four cases: the homogeneous medium with and without plasticity, and the fish bone structure with and without plasticity. The slope of these curves gives the rupture propagation speed for each case. The existence of the secondary branches significantly reduces the rupture speed compared to the homogeneous case. The rupture propagation speed generally decreases with off-fault plastic dissipation. The rupture propagates the slowest on the main fault for the case with fish bone structure in elasto-plastic medium. An unexpected observation is that with the existence of the secondary branches, the rupture may temporarily travel faster than the homogeneous case at first and then decelerate (See insert of

Fig. 9(a)). This may be explained by the fact that initially the rupture speed on the main fault is small, and that when these secondary branches are activated, they generate waves that may constructively interfere with the main rupture tip, channel energy to this tip, and promote its transient acceleration. As the main rupture accelerates further, this effect is diminished and the secondary faults act primarily as energy sinks, increasing the overall energy dissipation and decelerating the main fault rupture propagation. Once the rupture tip on the main fault moves beyond the fish bone region, it accelerates further approaching the propagation speed of the rupture in the homogeneous case with and without plasticity respectively.

Fig. 9(b) shows the maximum slip rate versus rupture tip position for the different cases. The secondary branches lead to a significant reduction in the peak slip rate on the main fault. Cases with off-fault plasticity also show a reduction in the peak slip rate compared to the elastic case. The existence of secondary branches also leads to high-frequency oscillations in the peak slip rate as the rupture propagates, indicative of enhanced radiation efficiency and high-frequency generation. After the rupture on the main fault has propagated beyond the region with the fish bone architecture, the peak slip rate increases and approaches the peak slip rate values for rupture propagation in the homogeneous medium.

Fig. 10 shows the main fault frictional energy dissipation normalized by the potency at each time step versus the average slip for the fish bone case and the homogeneous case with and without plasticity. The frictional dissipation is calculated by integrating the product of the frictional stress and the slip rate over the fault length and over time $E_f = \int_0^t (\int \tau_f \dot{D} da) dt'$. The potency is defined as the integral of the slip over the fault domain $P = \int D da$. The frictional dissipation normalized by the potency gives a stress-like quantity which may be taken indicative of an average frictional strength on the fault. Thus, the plots shown in Fig. 8 may be considered as modified effective slip-weakening laws for the fault as a whole. The homogeneous cases with and without plasticity have relatively similar effective stress-slip response. This is because the energy dissipated by off-fault plasticity is smaller than 0.1 percent of the frictional dissipation. Interestingly, the fish bone structure case with plasticity shows the least amount of frictional energy dissipation on the main fault of the four cases. This may be attributed to the other energy dissipation avenues that exist due to the combination of off-fault plasticity and frictional slip on the additional surfaces of the secondary faults. In particular, in the complex fish bone structure, the stress tends to be concentrated at the ends of the secondary faults leading to higher concentration of the plastic strain in this region. This increases the contribution to off-fault energy dissipation on the expense of the energy dissipation by frictional sliding on the main fault.

3.4 Parametric Study for the Elastic Case

In order to explore the effect of the secondary faults on the rupture characteristics of the main fault, we carried out a limited parametric study by varying some geometric properties of the secondary faults including length L_f , spacing L_s, and the angle with the main fault θ.

Effect of secondary fault length

Fig. 11 shows a snapshot of slip, slip rate, shear stress, and normal stress distribution on the main fault at a given instant of time. We examine three cases of secondary fault length $L_f = L_c$; $4L_c$; $6L_c$, while keeping all the other parameters the same as in the default case. With increased length of the secondary faults, the rupture speed on the main fault decreases as well as the maximum slip rate as shown in Fig. 11(b). However, the oscillations in the slip rate, shown in the insert in Fig. 11(b), increase with increasing the secondary faults length. Furthermore, Fig. 11(c) and Fig. 11(d) show that longer secondary faults promote a more complex pattern in the shear and normal stress perturbations. In particular, not all stress peaks or troughs have the same amplitude. This is because with longer secondary faults, slip is not necessarily accumulated through the whole length of each fault suggesting that some secondary faults may accumulate less slip or their rupture may stop before reaching the far end of the secondary fault. Fig. 12 shows the distribution of maximum slip on the secondary faults for different secondary fault length. The results suggest that as the secondary fault length increases, a crack shielding effect emerge; the slip distribution along the secondary faults is non-uniform in the sense that as one secondary fault accumulates large slip, the following one or two accumulate smaller slip, but then comes another secondary fault with large slip, and the pattern continues. The non-uniformity in slip that increases as the secondary fault length increases, leads to non-montonicity in the stress peaks on the main fault with some of the peaks smaller than others. This crack shielding-like phenomenon has been observed both in the experimental work by [Ngo et al.2012] for tensile cracks as well as numerical simulation results using finite-discrete element method by [Klinger et al.2018].

Effect of spacing distance between secondary faults

Fig. 13 shows a snapshot of slip, slip rate, shear stress, and normal stress distribution on the main fault at a given instant of time for three cases of secondary faults spacing $L_s = L_c$; $2L_c$; $4L_c$. As shown in Fig. 13(c) and 13(d), as the spacing between the secondary faults increases, the amplitude of perturbations in the shear and normal stresses on main fault increases since each secondary fault accumulates more slip on average than in the case of smaller spacing. With smaller spacing between the secondary faults, the secondary faults are more effective in decelerating the rupture on the main fault. The insert in Fig. 13(b) shows that with the increased spacing, the oscillations in the slip rate are spaced at a larger distance but their amplitude increases.

Effect of secondary fault angle with respect to the main fault

For the parameters shown in Table 1, the direction of optimally oriented shear plane makes approximately a 40 degree angle counterclockwise with the direction of the main fault. Here we consider three cases of orientation of the branching faults in addition to the default case discussed earlier: $\theta = 25^o$; 30^o; 40^o; 50^o. We focus primarily on the effect of secondary fault orientation on the stress perturbations on the main fault. Fig. 14 suggests that the amplitude of the shear and normal stress fluctuations on the main fault have a nonmonotonic trend as the secondary faults are rotated away from the main fault. The case for $\theta = 40^o$, which corresponds to optimally oriented shear plane, results in the largest amplitude of stress perturbations. This is also consistent with the observation that the secondary faults have larger slip values in this case (not shown here). As the secondary faults rotate away from this optimal direction, they accumulate less slip and also cause smaller stress perturbations on the main fault.

4 Discussion

Earthquake ruptures are nonlinear multiscale phenomena. The multiscale nature of the rupture process exists in both space and time. Spatially, a moderate-size earthquake typically propagates over tens of kilometres. However, the physical processes governing the rupture propagation operates within a narrow region at the rupture tip, called the process zone, which may not exceed a few millimetres in size if realistic laboratory-based friction parameters are used [Noda et al.2009]. Between these two distant limits, multiple intermediate scales exist and need to be resolved including shear bands, branches, foliations, kinks, and spatially varying damage zones both along strike and throughout depth. Temporally, an earthquake episode, where rapid slip occurs, only lasts for few to tens of seconds. However, the time required for stress buildup and the attainment of the right condition for the initiation of the friction instability during the interseismic period may be tens to hundreds of years [Lapusta et al.2000]. A fundamental challenge in earthquake source physics is to resolve this vast range of scales. In this paper we have focused on resolving the influence of one of the intermediate spatial scales, namely small scale fault branches, on the rupture dynamics of a single event. These branches are characterized as being small scale since their length is of the order of the reference length scale for nucleation in mature faults.

Our investigation of the effect of explicitly represented small scale branches on rupture dynamics reveals several results that are consistent with the more conventional method of modeling small scale damage as an effective elasto-plastic or continuum damage constitutive relation. For example, slip on these secondary faults increases the overall energy dissipation leading to a reduction in the accumulated slip, maximum slip rate, and rupture propagation speed on the main fault. However, explicit representation of these anisotropic pre-existing slip planes also lead to some novel insights that may not be captured by continuum plasticity models.

For example, the interaction of the main rupture with the short branches leads to strong heterogeneities in the final normal and shear stress distributions. These stress fluctuations may potentially lead to fault opening or reversal in the sign of the shear stress on the main fault, although this has not been observed within the parameter range explored in this paper. Interestingly, these stress heterogeneities due to the existence of the secondary branches persist even in the presence of elasto-plastic material response. They do not get smeared or homogenized. The nonuniform stress distribution left over after the seismic event may influence the nucleation, propagation, and arrest of future seismic events. Furthermore, the secondary branches may also act as potential nucleation sites for future ruptures, that do not lie directly on the main fault, but may potentially jump over to its plane. Thus, there is significant potential that this model may form a basis for earthquake complexity.

Moreover, explicit representation of the secondary branches suggest that these features may contribute significantly to the near field high frequency generation. The constructive interference between the seismic radiation from the secondary faults lead to coherent high-frequency generation in the bulk that is strongly correlated to the geometric distribution of the secondary branches. Furthermore, we demonstrated that the near-field acceleration spectrum in the presence of secondary faults is almost flat in the range of 2-20 Hz. This feature has been widely documented in observations [Wald and Heaton1994, Chen1995]. It is also similar to what [Dunham et al.2011b] have observed in dynamic rupture simulations on rough faults. This suggests that complex geometric features, other than fault roughness, such as secondary short branches, may lead to similar coherent high frequency generation patterns.

During dynamic rupture propagation, energy may be dissipated on the fault plane through frictional sliding or off the fault plane in bulk processes such as damage and plasticity. Explicitly introduced secondary branches, as done here, provide additional pathways for energy dissipation through frictional sliding on these planes. Furthermore, combining secondary branches with plasticity leads to an overall increase in energy dissipation. Interestingly, however, this overall increase in energy dissipation may be accompanied by a reduction in the effective energy dissipation through frictional sliding on the fault plane as illustrated in Fig. 10. Reduced frictional dissipation corresponds to potentially lower increase in the fault temperature and thus may contribute to resolving the heat flow paradox. This is a topic of future investigation.

Different mechanisms have been proposed for fault roughness evolution [Brodsky et al.2016, Ben-Zion and Sammis2003]. These mechanisms include fragmentation, wear, and healing. We have shown here that slip on secondary branches may lead to stress concentrations that load the main fault in a way that leads to undulations in the fault plane with a periodicity comparable to the spacing between the secondary branches. While the amplitude of these undulations is small, they may grow due to repeated ruptures, thus, providing an additional mechanism for fault plane roughness evolution on small scales.

In this paper, we have used linear slip-weakening as the fault constitutive model. Extensive field and laboratory observations suggest that friction is a more complicated function that does not depend directly on slip but rather on the instantaneous slip rate as well as the history of the slip rate. The rate and state formulation [Dieterich1979, Ruina1983] has been successful in interpreting several lab and field observations. While the slip-weakening friction may not be a realistic representation of the fault physics, it is a useful mathematical model. Furthermore, it may be shown that linear slip weakening friction may approximate rate and state friction response, without strong velocity weakening, with the appropriate choice of parameters. In future work, we plan to investigate our results in the framework of rate and state friction with dynamic weakening. This is crucial for extension to cycle simulations as well as in investigations of the role of large dynamic stress drops. Furthermore, it will be important to explore if time dependent post-seismic deformation may reduce the stress concentrations generated by the fish bone structure.

The parametric study conducted here related to the effect of secondary faults length, spacing, and orientation, provides new insights into how a main fault and a system of secondary faults may interact. We have found that a crack shielding phenomenon emerges as the length of the secondary faults in the sense that slip amplitude goes up and down along subsequent branches. Larger secondary fault length or larger spacing between the secondary faults generate stronger slip rate and stress perturbations and may lead to slower rupture propagation on the main fault. Secondary faults with orientation close to the direction of optimally oriented shear plane generate larger stress changes on the main fault than branches rotated away from the optimal directions. Similar effects on stress complexity were identified in a previous study on the effect of a single backthrust secondary fault on a main fault [Xu et al.2015b]. The hybrid scheme is enabling us to extend the explorations in this path by incorporating multiple secondary fault interactions with high resolutions.

The recent models by [Klinger et al.2018] provide a pioneering step towards exploration of the influence of co-seismically evolving off-fault damage on rupture dynamics. The current paper complements these on-going efforts in the community and provides a step forward towards explicit inclusion of small scale physics in fault zone in the form of pre-existing anisotropic damage features. Continuum damage models and conventional plasticity algorithms are prone to numerical localization. In our case, we pre-define the secondary slip planes based on the background tectonic stress field. While this biases our choice for the fault plane orientations, our results are not mesh dependent. There is a need for development of computational algorithms that may nucleate and grow faults on the fly with minimum or no mesh dependency. Potential candidates include nonlocal damage and plasticity models [Ma and Elbanna2018, Preuss et al.2019], extended finite element methods [Liu and Borja2009, Liu and Borja2013], and Discontinuous Galerkin scheme with adaptive mesh refinement [Pelties et al.2012, Pelties et al.2014].

In this paper, for modeling energy dissipation at scales smaller than the scale that is explicitly represented by the secondary branches, we adopted the rate-independent Drucker-Prager plasticity model. Without any regularization technique, the model is prone to artificial strain localization. While the stress concentration at the tips of the secondary branches is physical and necessitates a concentration in the plastic strain, a robust feature in our model that seems to persist at different resolutions, the orientation of the localization band shown in Fig. 8 around the tips of the fish bone structures may have a mesh-dependent ingredient. In the results presented here, the reported shear bands are several elements wide in some places but this does not entirely eliminate the mesh sensitivity. In future work, a rate-dependent plasticity model will be used such as rate-dependent Drucker-Prager plasticity model or rate sensitive Shear Transformation Zone theory [Ma and Elbanna2018] to avoid or limit the effects of any potential numerical artifacts.

In this paper we introduced an application of the recently developed hybrid method which attests to its potential for modeling dynamic rupture with high resolution fault zone physics. While explicit representation of short branches is a start, other candidate applications are also possible. For example, we may use the hybrid method to model strain localization and shear band evolution within the gouge region [Ma and Elbanna2018] while maintaining the influence of long range elastic stress transfer in the bulk. Another potential application is to model small-scale damage patterns, as has been done experimentally by [Biegel et al.2010] to study the transient and steady-state effect of damage patterns on the rupture dynamic. These problems are too challenging for the traditional domain-based numerical schemes but the efficient domain truncation using the hybrid scheme may make them more doable.

The characteristics of the hybrid method suggests that it may also potentially be used for long-duration earthquake cycle simulations on faults with near-field material heterogeneities, material nonlinearities, or fault surface complexities. The SBI formulation offers an accurate means for truncating the wave field in both dynamic and quasi-dynamic limits, making the hybrid method capable of capturing the effects of both seismic and interseismic phases of the cycle. Moreover, by exploiting the mode truncation and adaptive time-stepping techniques already embedded in the spectral formulation by Lapusta et al. [Lapusta et al.2000], it is possible to resolve the temporal multiscale nature of the rupture in an efficient manner. One can then envision coupling the SBI method with an implicit FEM scheme during the interseismic period to enable this extension. An outstanding challenge in modeling interseismic deformation on large scales is the need for efficient preconditioners for the large lineraized system of equations resulting from FEM. The hybrid method reduces the size of the domain to be discretized explicitly using the FEM and thus is expected to yield a smaller system of equations which may be solved efficiently and accurately using existing packages.

Future extensions of this work may include expanding the parametric study initiated here to include nonuniform spacing, orientation, and length of the secondary faults. It may also include exploration of the the effect of the strength parameter on interaction between the secondary branches and the main fault in terms of supershear susceptibility on either the main or secondary faults as well as scattering and interference of multiple Mach cones. The investigation may be extended to explore the influence of multiple scales and hierarchies of the secondary branches. The ultimate goal would be to use the hybrid scheme to model earthquake cycles in complex fault zone structures bridging both seismic and aseismic episodes and enabling the interplay between dynamics, stress evolution, and geometry to understand the underpinnings of earthquake complexity.

5 Conclusion

In this paper, we apply our recently developed hybrid numerical scheme to investigate the influence of explicitly represented small scale branches on rupture dynamics. This endeavor has been a challenge for most existing domain-based numerical methods. The complex interaction between the main fault rupture and the secondary fault branches is investigated. The results show the importance of considering near-fault complexities when performing dynamic rupture simulations. The main conclusions may be summarized as follows:

- The secondary faults increase the overall energy dissipation leading to a reduction in the slip, peak slip rate, and rupture propagation on the main fault.
- The activation of the secondary faults may lead to backward propagating ripples in the slip rate that increases slip far from the rupture tip.
- Rupture activation, propagation, and arrest on the secondary branches lead to a strongly heterogeneous normal and shear stress field on the main fault. These heterogeneities may potentially be large enough to cause fault opening or shear stress reversal. The complex post-event stress field would not have been generated using continuum plasticity models.
- The interaction of the seismic waves generated by the secondary branches promotes high-frequency generation and generate high-frequency fluctuations on the computed seismograms.
- The secondary branches lead to the evolution of normal undulations in the main fault strike.

Acknowledgment

The authors acknowledge support from the Center for Geologic Storage of CO2, an Energy Fronter Research Center funded by the U.S. Department of Energy (DOE), Office of Science, Basic Energy Sciences (BES), under Award #DE-SC0C12504, for development of the computational method. The authors also acknowledge support from the Southern California Earthquake Center through a collaborative agreement between NSF. Grant Number: EAR0529922 and USGS. Grant Number: 07HQAG0008 and the National Science Foundation CAREER award No 1753249 for modeling complex fault zone structures.

Appendix A Linear Elastic Fracture Mechanics analysis on the stress perturbation on the main fault

Here we present an example calculation of using Linear Elastic Fracture Mechanics to predict the stress perturbation pattern on the main fault due to the presence of a secondary fault in its vicinity. We idealize the secondary fault as a Mode II finite length crack in an infinite domain. From [Sun and Jin2012], the stress distribution around the crack tip in this case is given by Eq. A.1

$$\begin{aligned}
\sigma_{xx} &= -\frac{K_{II}}{\sqrt{2\pi r}} \sin\frac{\phi}{2}(2+\cos\frac{\phi}{2}\cos\frac{3\phi}{2}) \\
\sigma_{yy} &= \frac{K_{II}}{\sqrt{2\pi r}} \sin\frac{\phi}{2}\cos\frac{\phi}{2}\cos\frac{3\phi}{2} \\
\sigma_{xy} &= \frac{K_{II}}{\sqrt{2\pi r}} \cos\frac{\phi}{2}(1-\sin\frac{\phi}{2}\sin\frac{3\phi}{2})
\end{aligned} \tag{A.1}$$

where K_{II} is the stress intensity factor for Mode II fracture. ϕ and r are the angle and radius in the polar coordinate system. The geometry model is defined as shown in Fig. A.1.

From Eq. A.1, we compute the stress tensor σ from which we may compute the normal traction component σ_n and the tangential component τ on the main fault as given by Eq. A.2:

$$\begin{aligned}
\mathbf{T} &= \sigma\mathbf{n} \\
\sigma_N &= \mathbf{T}\cdot\mathbf{n} \\
\tau &= \sqrt{|\mathbf{T}|^2 - \sigma_N}
\end{aligned} \tag{A.2}$$

Where $\mathbf{n}$ is the vector normal to plane of the main fault. The results are plotted in Fig. A.2, and give a pattern for the stress perturbation expected from a branch that qualitatively agrees with the numerical results shown in the paper.

References

[Ando and Yamashita2007] Ando, R. and Yamashita, T. (2007). Effects of mesoscopic-scale fault structure on dynamic earthquake ruptures: Dynamic formation of geometrical complexity of earthquake faults. *Journal of Geophysical Research*, 112(B9):B09303.

[Andrews1976] Andrews, D. J. (1976). Rupture propagation with finite stress in antiplane strain. *Journal of Geophysical Research*, 81(20):3575.

[Andrews2005] Andrews, D. J. (2005). Rupture dynamics with energy loss outside the slip zone. *Journal of Geophysical Research*, 110(B1):B01307.

[Ben-Zion and Sammis2003] Ben-Zion, Y. and Sammis, C. G. (2003). Characterization of Fault Zones. *Pure and Applied Geophysics*, 160(3):677–715.

[Ben-Zion and Shi2005] Ben-Zion, Y. and Shi, Z. (2005). Dynamic rupture on a material interface with spontaneous generation of plastic strain in the bulk. *Earth and Planetary Science Letters*, 236(1-2):486–496.

[Berenger1994] Berenger, J.-P. (1994). A perfectly matched layer for the absorption of electromagnetic waves.

[Bettess1977] Bettess, P. (1977). Infinite elements. *International Journal for Numerical Methods in Engineering*, 11(1):53–64.

[Bhat et al.2004] Bhat, H. S., Dmowska, R., Rice, J. R., and Kame, N. (2004). Dynamic slip transfer from the Denali to totschunda faults, Alaska: Testing theory for fault branching. *Bulletin of the Seismological Society of America*, 94(6 SUPPL. B):202–213.

[Bhat et al.2012] Bhat, H. S., Rosakis, A. J., and Sammis, C. G. (2012). A Micromechanics Based Constitutive Model for Brittle Failure at High Strain Rates. *Journal of Applied Mechanics*, 79(3):031016.

[Biegel et al.2010] Biegel, R., Bhat, H., Sammis, C., and Rosakis, A. (2010). The effect of asymmetric damage on dynamic shear rupture propagation I: No mismatch in bulk elasticity. *Tectonophysics*, 493(3-4):254–262.

[Biegel et al.2007] Biegel, R. L., Sammis, C. G., and Rosakis, A. J. (2007). Interaction of a Dynamic Rupture on a Fault Plane with Short Frictionless Fault Branches. *Pure and Applied Geophysics*, 164(10):1881–1904.

[Bielak et al.2003] Bielak, J., Loukakis, K., Hisada, Y., and Yoshimura, C. (2003). Domain Reduction Method for Three-Dimensional Earthquake Modeling in Localized Regions, Part I: Theory. *Bulletin of the Seismological Society of America*, 93(2):817–824.

[Brodsky et al.2016] Brodsky, E. E., Kirkpatrick, J. D., and Candela, T. (2016). Constraints from fault roughness on the scale-dependent strength of rocks. *Geology*, 44(1):19–22.

[Chen1995] Chen, X. (1995). Near-field ground motion from the Landers earthquake.

[Chester et al.1993] Chester, F. M., Evans, J. P., and Biegel, R. L. (1993). Internal structure and weakening mechanisms of the San Andreas Fault. *Journal of Geophysical Research: Solid Earth*, 98(B1):771–786.

[Das and Aki1977] Das, S. and Aki, K. (1977). A numerical study of two-dimensional spontaneous rupture propagation. *Geophysical Journal International*, 50(3):643–668.

[Day1982] Day, S. M. (1982). Three-dimensional finite difference simulation of fault dynamics: Rectangular faults with fixed rupture velocity. *Bulletin of the Seismological Society of America*, 72(3):705–727.

[DeDontney et al.2012] DeDontney, N., Rice, J. R., and Dmowska, R. (2012). Finite Element Modeling of Branched Ruptures Including Off-Fault Plasticity. *Bulletin of the Seismological Society of America*, 102(2):541–562.

[Dieterich1979] Dieterich, J. H. (1979). Modeling of rock friction: 1. Experimental results and constitutive equations. *Journal of Geophysical Research: Solid Earth*, 84(B5):2161–2168.

[Drucker and Prager1952] Drucker, D. C. and Prager, W. (1952). Soil mechanics and plastic analysis or limit design. *Quarterly of Applied Mathematics*, 10(2):157–165.

[Dunham et al.2011a] Dunham, E. M., Belanger, D., Cong, L., and Kozdon, J. E. (2011a). Earthquake Ruptures with Strongly Rate-Weakening Friction and Off-Fault Plasticity, Part 1: Planar Faults. *Bulletin of the Seismological Society of America*, 101(5):2296–2307.

[Dunham et al.2011b] Dunham, E. M., Belanger, D., Cong, L., and Kozdon, J. E. (2011b). Earthquake ruptures with strongly rate-weakening friction and off-fault plasticity, part 2: Nonplanar faults. *Bulletin of the Seismological Society of America*, 101(5):2308–2322.

[Duru and Dunham2016] Duru, K. and Dunham, E. M. (2016). Dynamic earthquake rupture simulations on nonplanar faults embedded in 3D geometrically complex, heterogeneous elastic solids. *Journal of Computational Physics*, 305(C):185–207.

[Geubelle1995] Geubelle, Philipppe H., R.-J. R. (1995). A Spectral Method for Three-Dimensional Fracture Problems. *Journal of the Mechanics and Physics of Solids*, 43(11):1791–1824.

[Hajarolasvadi and Elbanna2017] Hajarolasvadi, S. and Elbanna, A. E. (2017). A new hybrid numerical scheme for modelling elastodynamics in unbounded media with near-source heterogeneities. *Geophysical Journal International*, 211(2):851–864.

[Hok et al.2010] Hok, S., Campillo, M., Cotton, F., Favreau, P., and Ionescu, I. (2010). Off-fault plasticity favors the arrest of dynamic ruptures on strength heterogeneity: Two-dimensional cases. *Geophysical Research Letters*, 37(2):n/a–n/a.

[Ida1972] Ida, Y. (1972). Cohesive force across the tip of a longitudinal-shear crack and Griffith's specific surface energy. *Journal of Geophysical Research*, 77(20):3796–3805.

[Kame et al.2003] Kame, N., Rice, J. R., and Dmowska, R. (2003). Effects of prestress state and rupture velocity on dynamic fault branching. *Journal of Geophysical Research: Solid Earth*, 108(B5):1–21.

[Klinger et al.2018] Klinger, Y., Okubo, K., Vallage, A., Champenois, J., Delorme, A., Rougier, E., Lei, Z., Knight, E. E., Munjiza, A., Satriano, C., Baize, S., Langridge, R., and Bhat, H. S. (2018). Earthquake Damage Patterns Resolve Complex Rupture Processes. *Geophysical Research Letters*, pages 279–287.

[Lapusta et al.2000] Lapusta, N., Rice, J. R., Ben-Zion, Y., and Zheng, G. (2000). Elastodynamic analysis for slow tectonic loading with spontaneous rupture episodes on faults with rate- and state-dependent friction. *Journal of Geophysical Research*, 105:23765.

[Liu and Borja2009] Liu, F. and Borja, R. I. (2009). An extended finite element framework for slow-rate frictional faulting with bulk plasticity and variable friction. *International Journal for Numerical and Analytical Methods in Geomechanics*, 33(13):1535–1560.

[Liu and Borja2013] Liu, F. and Borja, R. I. (2013). Extended finite element framework for fault rupture dynamics including bulk plasticity. *International Journal for Numerical and Analytical Methods in Geomechanics*, 37(18):3087–3111.

[Liu and Lapusta2008] Liu, Y. and Lapusta, N. (2008). Transition of mode II cracks from sub-Rayleigh to intersonic speeds in the presence of favorable heterogeneity. *Journal of the Mechanics and Physics of Solids*, 56(1):25–50.

[Lysmer and Kuhlemeyer1969] Lysmer, J. and Kuhlemeyer, R. L. (1969). Finite dynamic model for infinite media. *journal of Engineering Mechanics Division*, 95:859–878.

[Ma and Elbanna2018] Ma, X. and Elbanna, A. (2018). Strain localization in dry sheared granular materials: A compactivity-based approach. *Phys. Rev. E*, 98(2):22906.

[Ma et al.2018] Ma, X., Hajarolasvadi, S., Albertini, G., Kammer, D. S., and Elbanna, A. E. (2018). A hybrid finite element-spectral boundary integral approach: Applications to dynamic rupture modeling in unbounded domains. *International Journal for Numerical and Analytical Methods in Geomechanics*, (August):1–22.

[Ngo et al.2012] Ngo, D., Huang, Y., Rosakis, A., Griffith, W. A., and Pollard, D. (2012). Off-fault tensile cracks: A link between geological fault observations, lab experiments, and dynamic rupture models. *Journal of Geophysical Research: Solid Earth*, 117(B1):n/a–n/a.

[Noda et al.2009] Noda, H., Dunham, E. M., and Rice, J. R. (2009). Earthquake ruptures with thermal weakening and the operation of major faults at low overall stress levels. *Journal of Geophysical Research*, 114(B7):B07302.

[Pelties et al.2012] Pelties, C., de la Puente, J., Ampuero, J.-P., Brietzke, G. B., and Käser, M. (2012). Three-dimensional dynamic rupture simulation with a high-order discontinuous Galerkin method on unstructured tetrahedral meshes. *Journal of Geophysical Research: Solid Earth*, 117(B2):n/a–n/a.

[Pelties et al.2014] Pelties, C., Gabriel, A.-A., and Ampuero, J.-P. (2014). Verification of an ADER-DG method for complex dynamic rupture problems. *Geoscientific Model Development*, 7(3):847–866.

[Poliakov et al.2002] Poliakov, A. N. B., Dmowska, R., and Rice, J. R. (2002). Dynamic shear rupture interactions with fault bends and off-axis secondary faulting. *Journal of Geophysical Research*, 107(B11):ESE 6–1–ESE 6–18.

[Preuss et al.2019] Preuss, S., Herrendörfer, R., Gerya, T., Ampuero, J.-P., and Dinther, Y. v. (2019). Seismic and aseismic fault growth lead to different fault orientations. *EarthArXiv*.

[Rempe et al.2013] Rempe, M., Mitchell, T., Renner, J., Nippress, S., Ben-Zion, Y., and Rockwell, T. (2013). Damage and seismic velocity structure of pulverized rocks near the San Andreas Fault. *Journal of Geophysical Research: Solid Earth*, 118(6):2813–2831.

[Rousseau and Rosakis2009] Rousseau, C.-E. and Rosakis, A. J. (2009). Dynamic path selection along branched faults: Experiments involving sub-Rayleigh and supershear ruptures. *Journal of Geophysical Research*, 114(B8):B08303.

[Rowe et al.2018] Rowe, C. D., Ross, C., Swanson, M. T., Pollock, S., Backeberg, N. R., Barshi, N. A., Bate, C. E., Carruthers, S., Coulson, S., Dascher-Cousineau, K., Harrichhausen, N., Peña Castro, A. F., Nisbet, H., Rakoczy, P., Scibek, J., Smith, H., Tarling, M. S., Timofeev, A., and Young, E. (2018). Geometric Complexity of Earthquake Rupture Surfaces Preserved in Pseudotachylyte Networks. *Journal of Geophysical Research: Solid Earth*, 123(9):7998–8015.

[Rudnicki and Rice1975] Rudnicki, J. W. and Rice, J. R. (1975). Conditions for the localization of deformation in pressure-sensitive dilatant materials. *Journal of the Mechanics and Physics of Solids*, 23(6):371–394.

[Ruina1983] Ruina, A. (1983). Slip instability and state variable friction laws. *Journal of Geophysical Research: Solid Earth*, 88(B12):10359–10370.

[Savage and Brodsky2011] Savage, H. M. and Brodsky, E. E. (2011). Collateral damage: Evolution with displacement of fracture distribution and secondary fault strands in fault damage zones. *Journal of Geophysical Research: Solid Earth*, 116(3).

[Shi and Day2013] Shi, Z. and Day, S. M. (2013). Rupture dynamics and ground motion from 3-D rough-fault simulations. *Journal of Geophysical Research: Solid Earth*, 118(3):1122–1141.

[Sowers et al.1911] Sowers, J. M., Unruh, J. R., Lettis, W. R., and Rubin, T. D. (1911). Relationship of the kickapoo fault to the Johnson Valley and Homestead Valley faults, San Bernardino County, California. *Bulletin of the Seismological Society of America*, 84(3):528–536.

[Sun and Jin2012] Sun, C. T. C.-T. and Jin, Z.-H. (2012). *Fracture mechanics*. Academic Press.

[Suzuki2013] Suzuki, T. (2013). Damage-tensor-based nondimensional parameters governing secondary faulting behavior. *Tectonophysics*, 600:205–216.

[Tal et al.2018] Tal, Y., Hager, B. H., and Ampuero, J. P. (2018). The Effects of Fault Roughness on the Earthquake Nucleation Process. *Journal of Geophysical Research: Solid Earth*, 123(1):437–456.

[Templeton and Rice2008] Templeton, E. L. and Rice, J. R. (2008). Off-fault plasticity and earthquake rupture dynamics: 1. Dry materials or neglect of fluid pressure changes. *Journal of Geophysical Research: Solid Earth*, 113(9):1–19.

[Uenishi and Rice2003] Uenishi, K. and Rice, J. R. (2003). Universal nucleation length for slip-weakening rupture instability under nonuniform fault loading. *Journal of Geophysical Research: Solid Earth*, 108(B1).

[Uphoff et al.2017] Uphoff, C., Rettenberger, S., Bader, M., Madden, E. H., Ulrich, T., Wollherr, S., and Gabriel, A.-A. (2017). Extreme scale multi-physics simulations of the tsunamigenic 2004 sumatra megathrust earthquake. In *Proceedings of the International Conference for High*

Performance Computing, Networking, Storage and Analysis on - SC '17, pages 1–16, New York, New York, USA. ACM Press.

[Wald and Heaton1994] Wald, D. J. and Heaton, T. H. (1994). Spatial and temporal distribution of slip for the 1992 Landers, California, earthquake. *Bulletin of the Seismological Society of America*, 84(3):668–691.

[Xu et al.2015a] Xu, S., Ben-Zion, Y., Ampuero, J. P., and Lyakhovsky, V. (2015a). Dynamic Ruptures on a Frictional Interface with Off-Fault Brittle Damage: Feedback Mechanisms and Effects on Slip and Near-Fault Motion. *Pure and Applied Geophysics*.

[Xu et al.2015b] Xu, S., Fukuyama, E., Ben-Zion, Y., and Ampuero, J.-P. (2015b). Dynamic rupture activation of backthrust fault branching. *Tectonophysics*, 644-645:161–183.

[Yoshimura et al.2003] Yoshimura, C., Bielak, J., Hisada, Y., and Fernańdez, A. (2003). Domain Reduction Method for Three-Dimensional Earthquake Modeling in Localized Regions, Part II: Verification and Applications. *Bulletin of the Seismological Society of America*, 93(2):825–841.

Tables

Medium Material Properties	**Value**
Shear Modulus μ	32 GPa
S wave velocity c_s	3.464 $km \cdot s^{-1}$
P wave velocity c_p	6.0 $km \cdot s^{-1}$
Angle of Internal Friction ψ	30.96^o
Maximum Principle Stress direction θ_p	19.33^o
Fault constitutive Parameters	**Value**
Static friction coefficient μ_s	0.6
Dynamic friction coefficient μ_d	0.3
Characteristic slip-weakening distance d_c	0.2 m
Background Stress	**Value**
Background Vertical Stress σ_{yy}	-50.0 MPa
Background Horizontal Stress σ_{xx}	-100.0 MPa
Background Shear Stress σ_{xy}	20.0 MPa
Domain Geometry	**Value**
Reference length scale L_c	500 m
Length of the secondary faults L_f	Varies
Spacing between the secondary faults L_s	Varies
The off distance of the secondary fault from the main fault L_o	0.1L_c
The angle between the secondary fault and the main fault θ_n	Varies
Finite element cell size h	6.25m

Table 1: Parameters Description

834 Figures

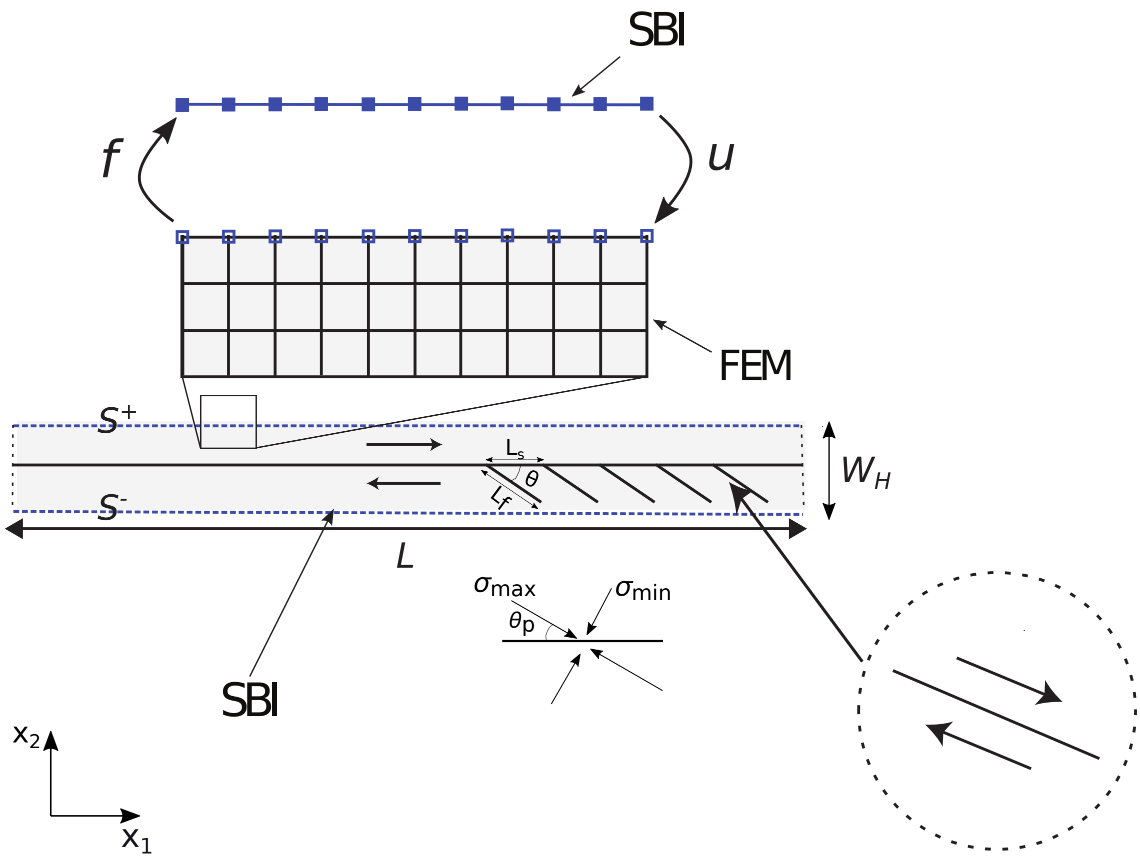

Figure 1: Schematic of the complex fault zone structure considered in this paper. The main fault lies horizontally in the middle of the domain, and the secondary branches are located in a limited region on one side of the fault (tension side). Following [Poliakov et al.2002] we call this setup a fish bone structure. All secondary faults are contained in a narrow virtual strip of dimensions L $\times$ W that is discretized using the Finite element method (FEM). On the upper and lower edges S^+ and S^-, the FEM is coupled with the Spectral Boundary Integral Equation which exactly model the exterior homogeneous elastic half spaces. Tractions and displacements are consistently exchanged between the two methods at the shared nodes. The details of the coupling is outlined in the text. σ_{max} and σ_{min} represents the maximum and minimum principle stresses respectively. θ_p is the angle between the maximum principle stress and the main fault parallel direction. L_s is the spacing between the secondary fault, θ is the angle between the secondary fault and the main fault. L_f is the secondary fault length.

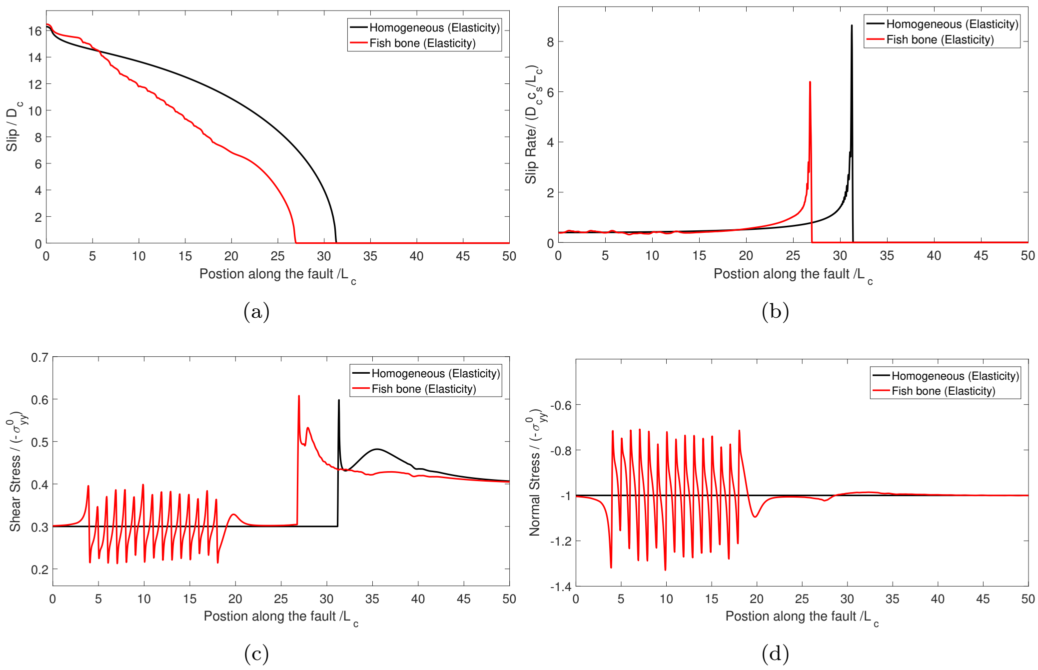

Figure 2: Slip, slip rate, shear stress and normal stress distributions on the main fault, at the same point in time, with and without secondary branches for the elastic material case. (a) Slip, (b) Slip rate, (c) Shear stress distribution, and (d) Normal stress distribution. Overall, the fish bone case shows significant post-event stress heterogeneities as well as reduced slip, maximum slip rate, and rupture speed. The full time history for the evolution of the slip, slip rate, and shear stress on the main fault is included in Supplementary Material 1.

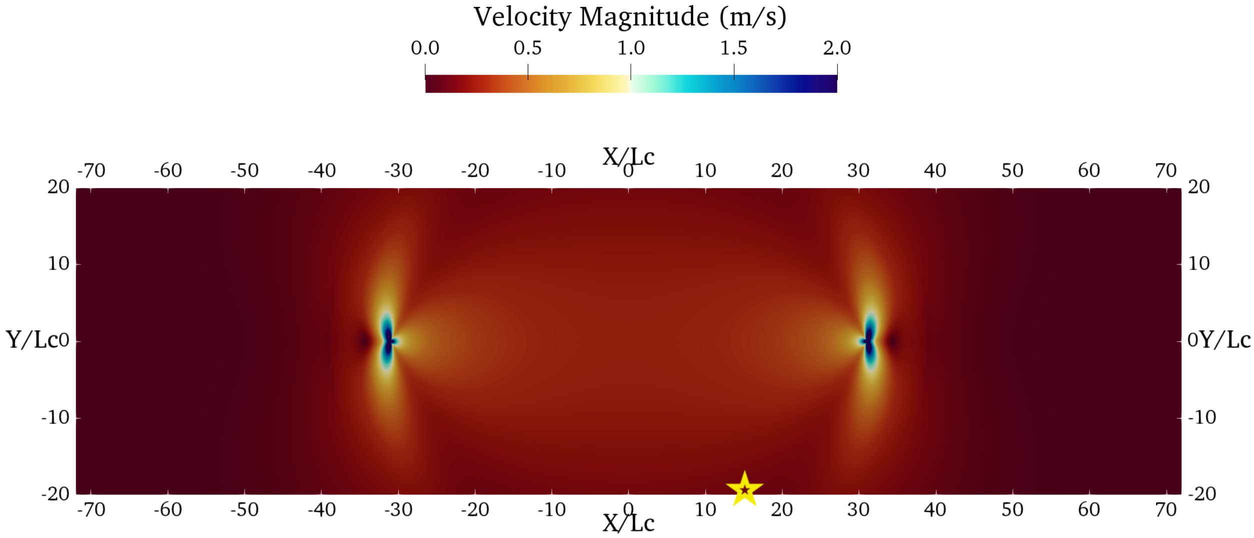

(a)

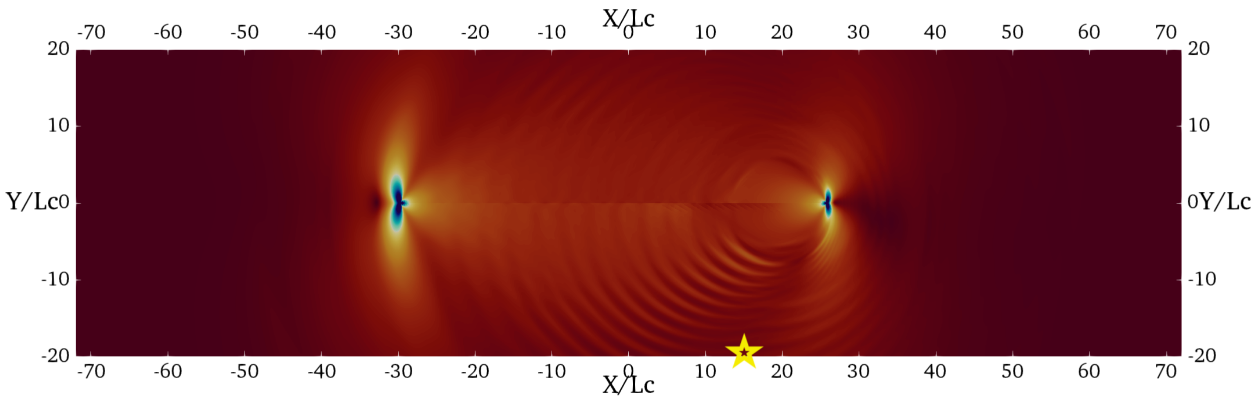

(b)

Figure 3: Contours of the bulk velocity field. (a) Homogeneous medium. (b) Domain with fish bone structure. Coherent high frequency generation emerge in the case of the fault with secondary branches (fish bone structure) and propagate away from the fault plane as concentric fringes. These high frequency waves are generated as a result of the constructive interference between the waves emitted by the the secondary branches. In the homogeneous case the high frequency wave field is localized near the rupture fronts. We have also included videos for the process of high frequency generation in Supplementary Materials 2 and 3.

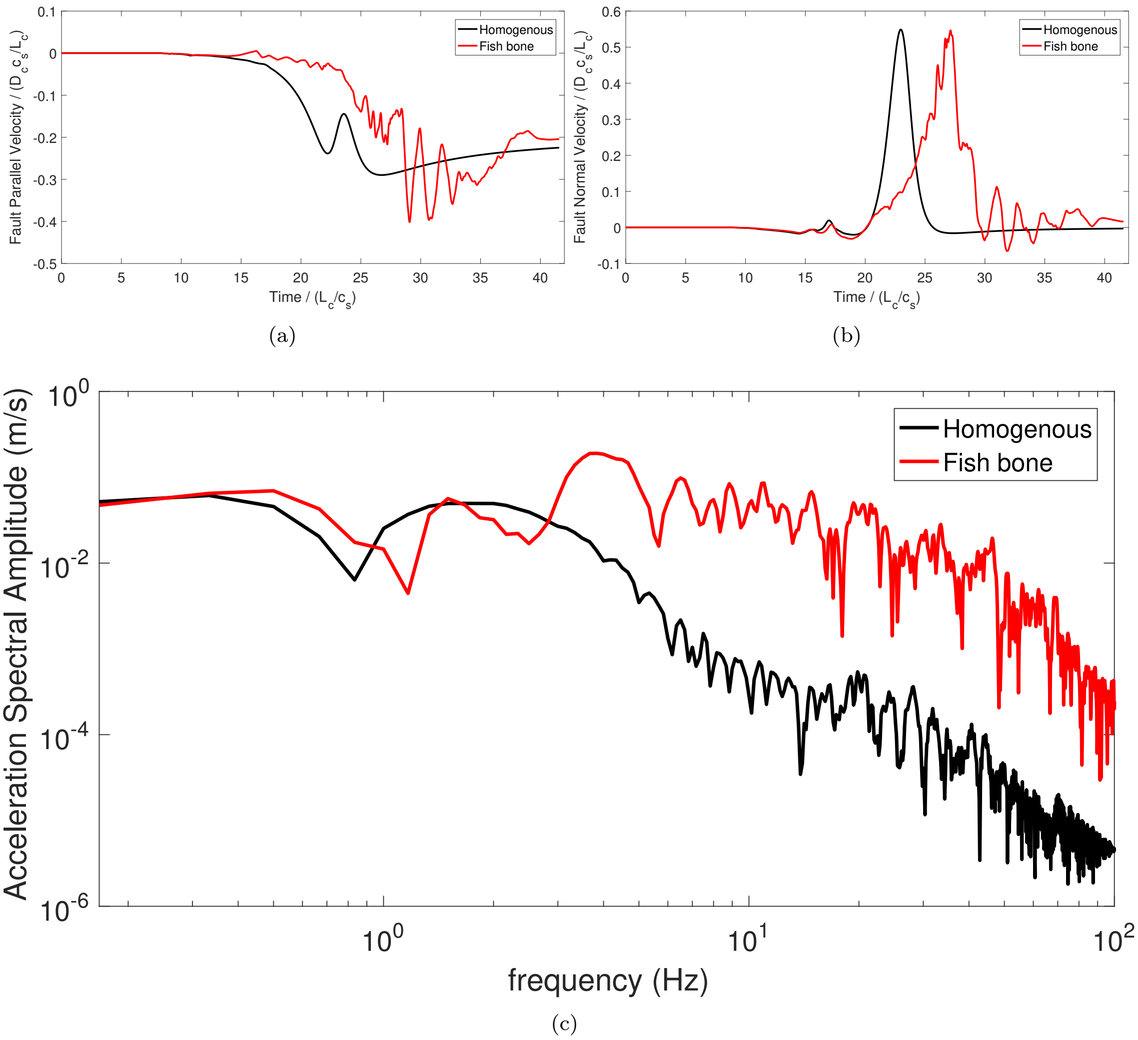

Figure 4: High frequency generation with and without secondary branches. (a),(b) Fault-parallel and fault-normal velocities at a station located at $x* = 15L_c$ and $y^* = -2L_c$ (c) fault-normal acceleration spectral amplitude at station $x* = 15L_c$ and $y^* = -2L_c$.

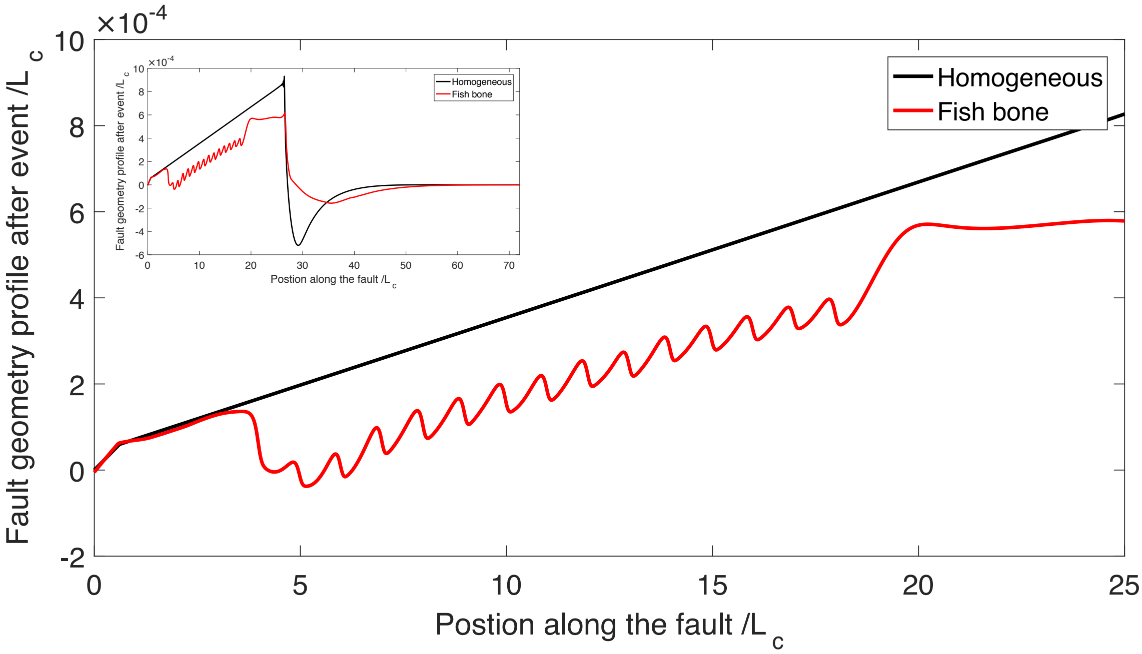

Figure 5: Normal displacement distribution with and without secondary branches. The insert figure shows the whole distribution along the full half length of the fault. The secondary faults cause periodic undulations in the main fault profile

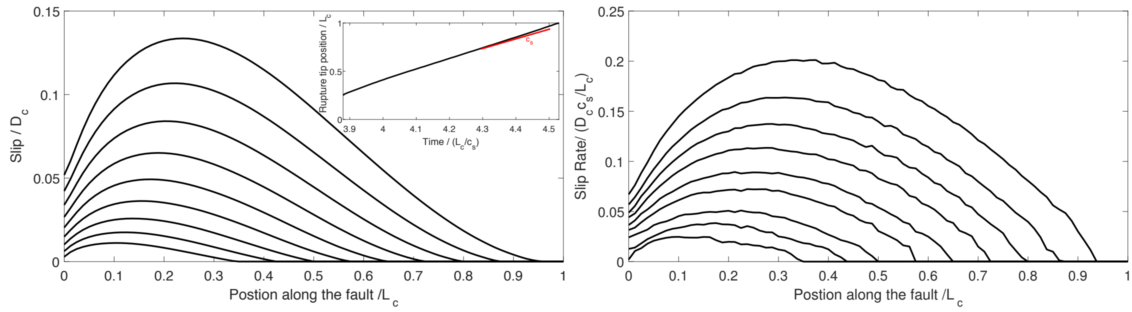

(a) (b)

Figure 6: Slip and slip rate distributions on the first secondary fault at consecutive time steps (plotted every 0.02s). (a) Slip, (b) Slip rate. Insert figure in (a) shows the rupture tip position along the secondary fault versus time suggesting that the rupture is propagating at supershear speeds.

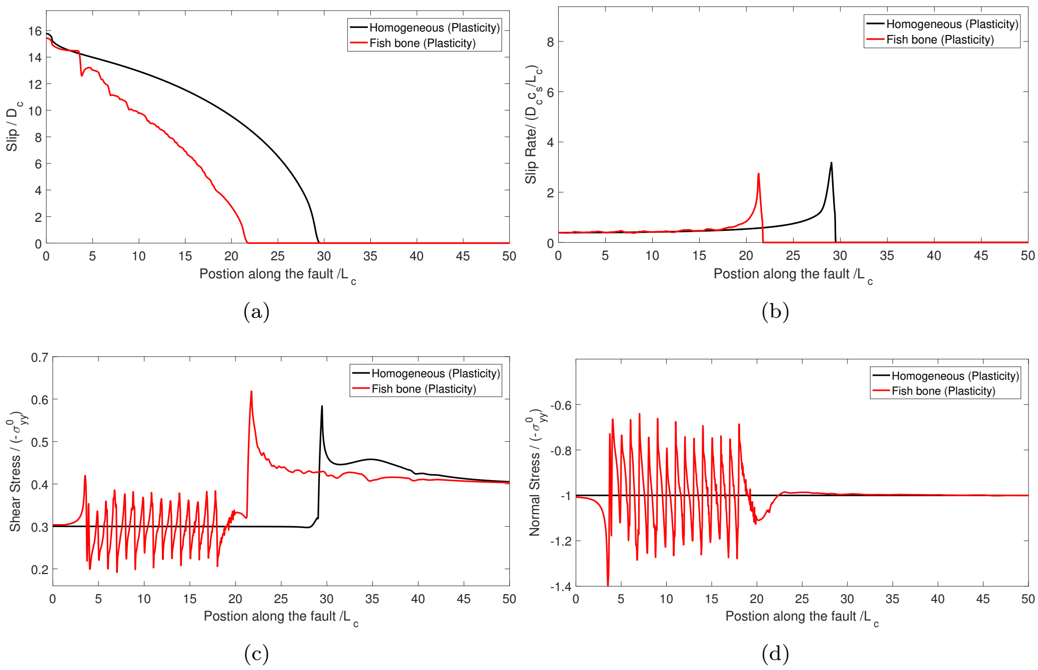

Figure 7: Slip, slip rate, shear stress, and normal stress distributions on the main fault, at the same point in time, with and without secondary branches for the elasto-plastic material case. (a) Slip, (b) Slip rate, (c) Shear stress distribution, and (d) Normal stress distribution. Overall, the fish bone case shows significant post-event stress heterogeneities as well as reduced slip, maximum slip rate, and rupture speed. The values of slip and maximum slip rate in the elasto-plastic case are lower than the elastic case.

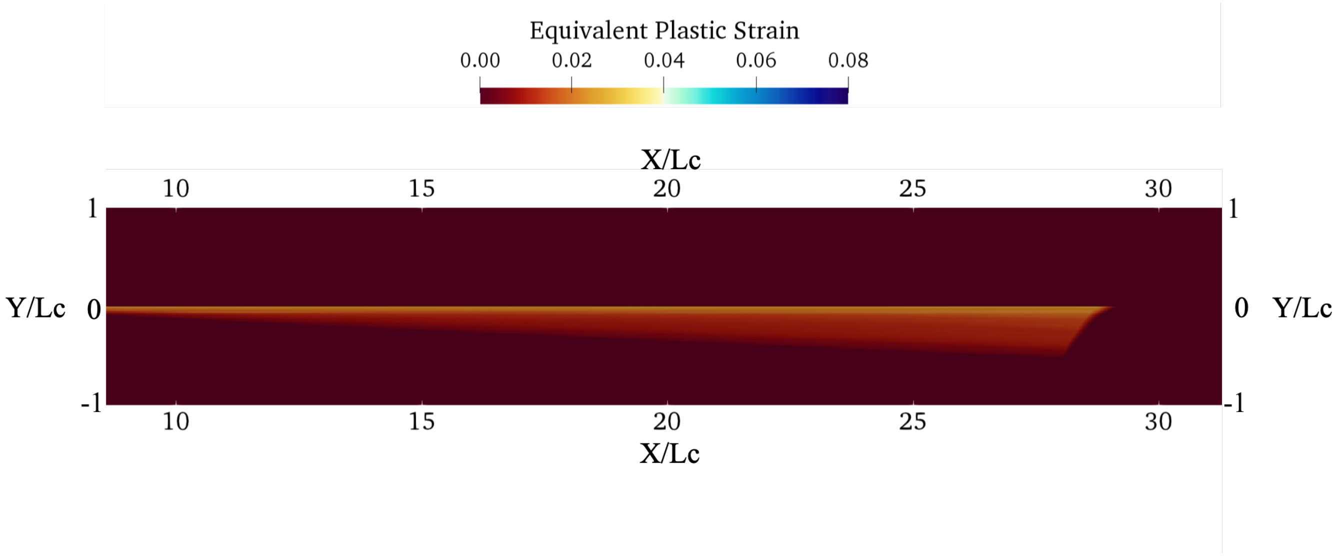

(a)

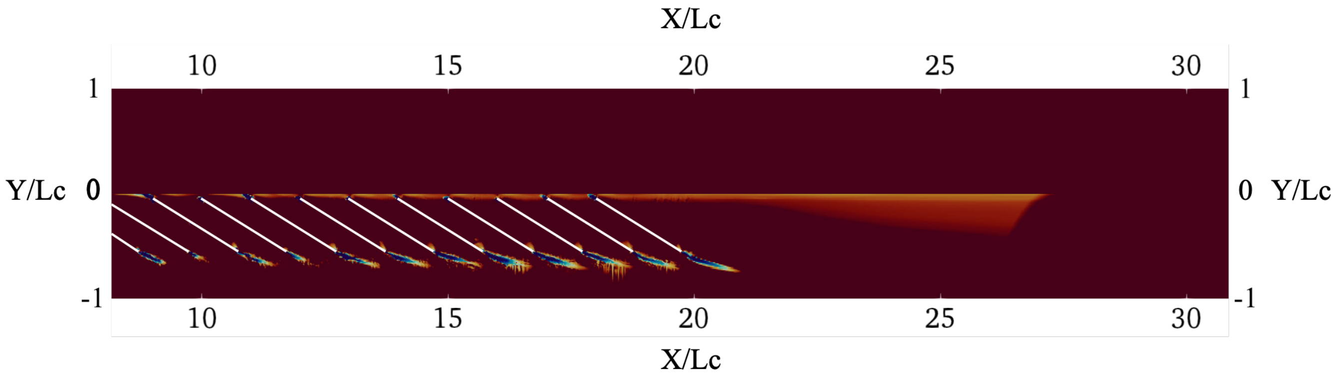

(b)

Figure 8: Equivalent Plastic Strain distribution (a) Homogeneous material (b) Fish bone structure. The lines in white are the location of the secondary branches.

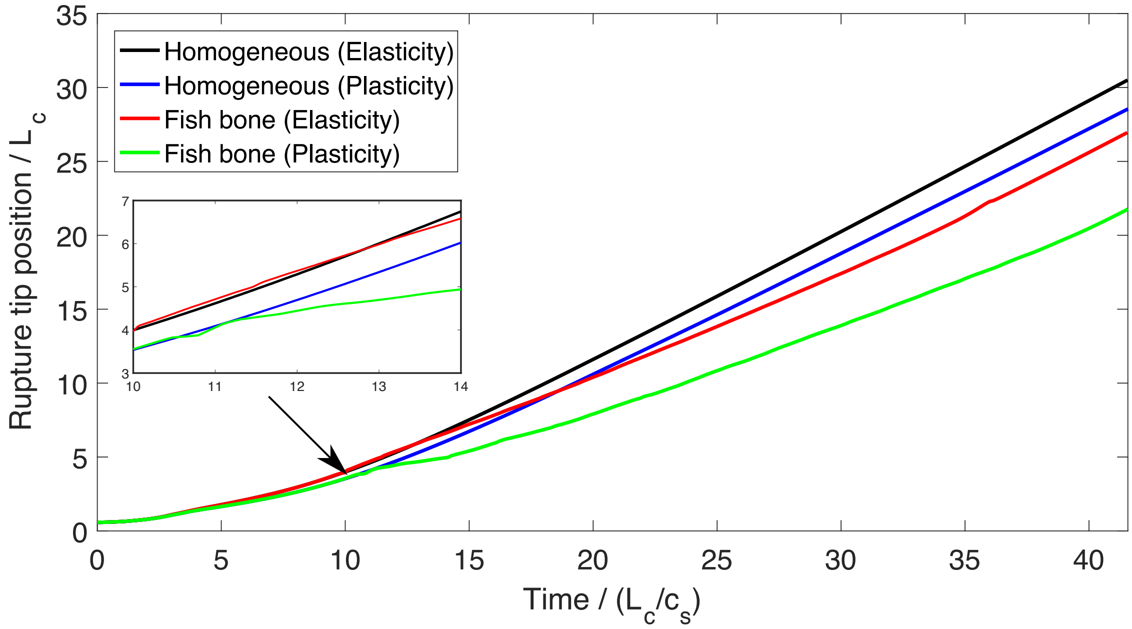

(a)

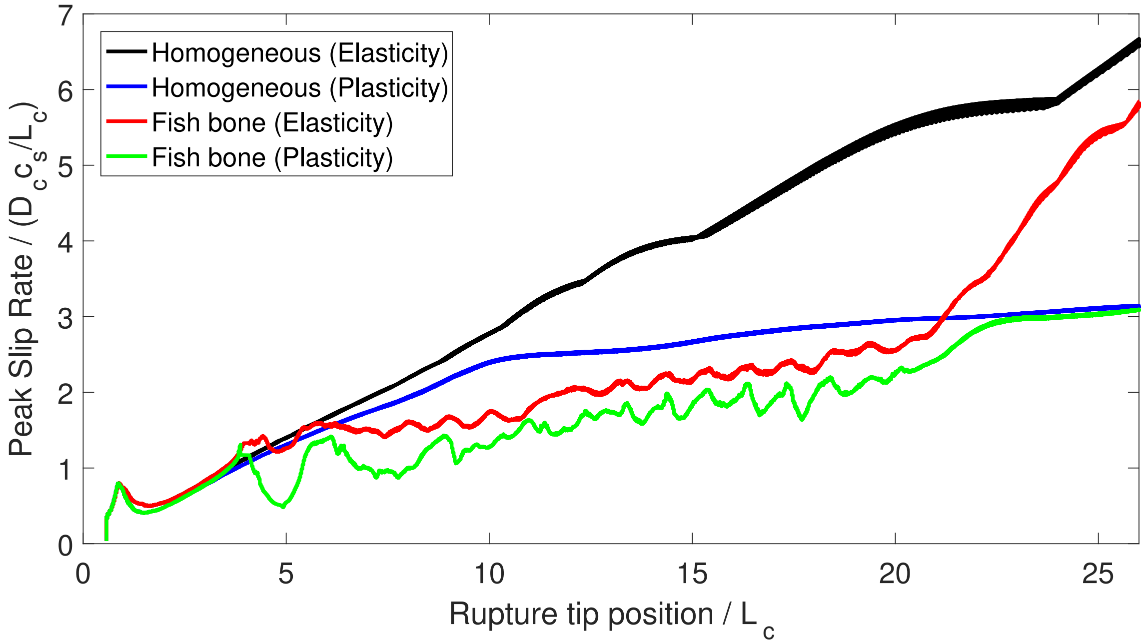

(b)

Figure 9: Comparison of rupture characteristics in the different cases (a) Rupture Tip position on the main fault as a function of time for the homogeneous and fish bone cases with elastic and elasto-plastic material models (b) Peak slip rate as a function of rupture tip position on the main fault for homogeneous and fish bone cases with elastic and elastoplastic material models

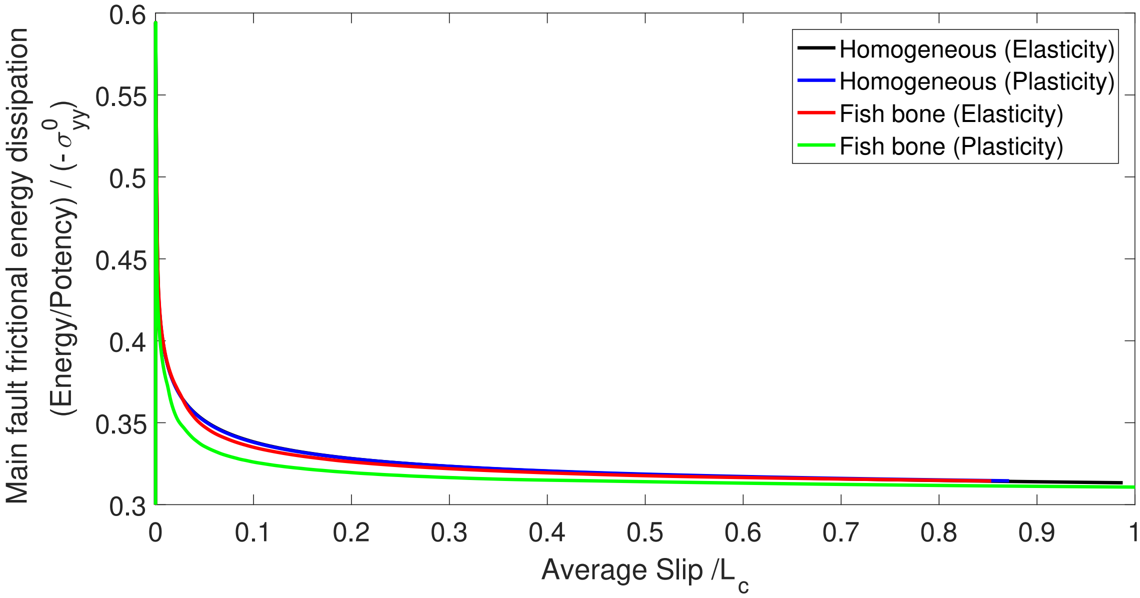

Figure 10: Frictional dissipation normalized by potency for the main fault in the four different different cases investigated in the manuscript. The homogeneous case with either elastic or elasto-plastic material models shows similar normalized frictional energy dissipation. The fish bone structure with elastic material has lower normalized frictional dissipation on the main fault than the homogeneous case due to off-fault energy dissipation by frictional sliding on the secondary branches. The fish bone structure with plasticity dissipate the least energy on the main fault as frictional heat among the four cases because more energy is being dissipated by the localized plastic deformation at the tips of the secondary faults.

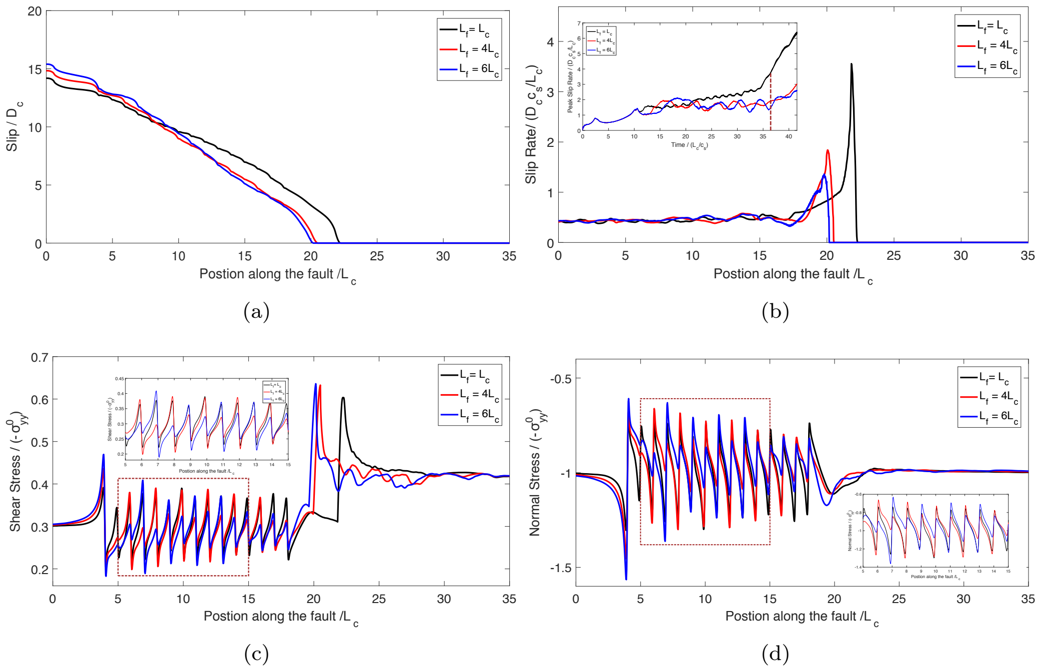

Figure 11: Slip, slip rate, shear stress, and normal stress distributions on the main fault, at the same point in time, with different lengths of secondary faults $L_f = L_c, 4L_c, 6L_c$ for the elastic material case. (a) Slip, (b) Slip rate, (c) Shear stress distribution, and (d) Normal stress distribution. Longer secondary faults promote a more complex pattern of stress perturbations on the main fault and lead to further reduction in the main rupture propagation speed.

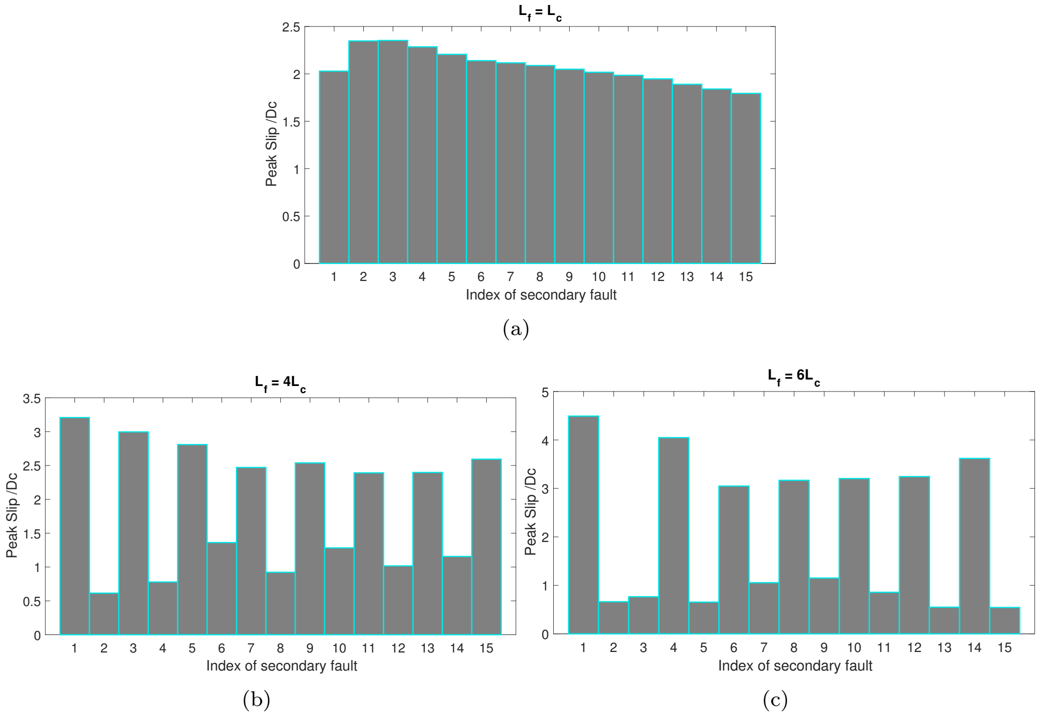

Figure 12: Peak Slip distribution on the secondary faults with different length $L_f = L_c$ $L_f = 4L_c$ and $L_f = 6L_c$. The crack shielding effect is more significant in the presence of longer secondary faults.

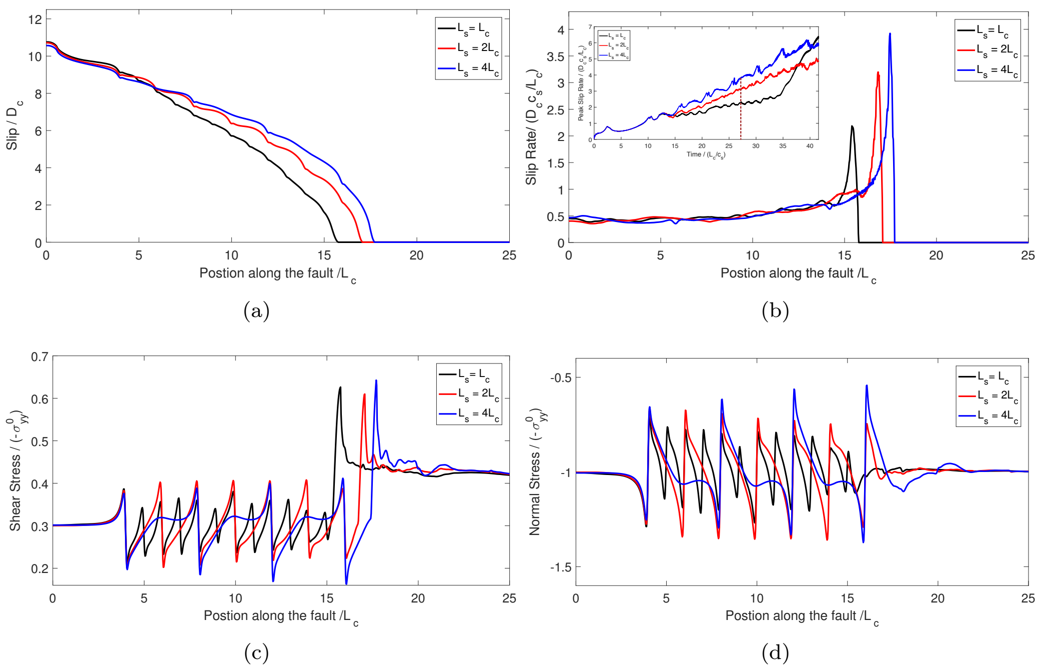

Figure 13: Slip, slip rate, shear stress, and normal stress distributions on the main fault, at the same point in time, with different spacing between the secondary faults $L_s = L_c, 2L_c, 4L_c$for the elastic material case. (a) Slip, (b) Slip rate, (c) Shear stress distribution, and (d) Normal stress distribution. Larger spacing between secondary faults promote stronger perturbations in the stress and slip rate on the main fault.

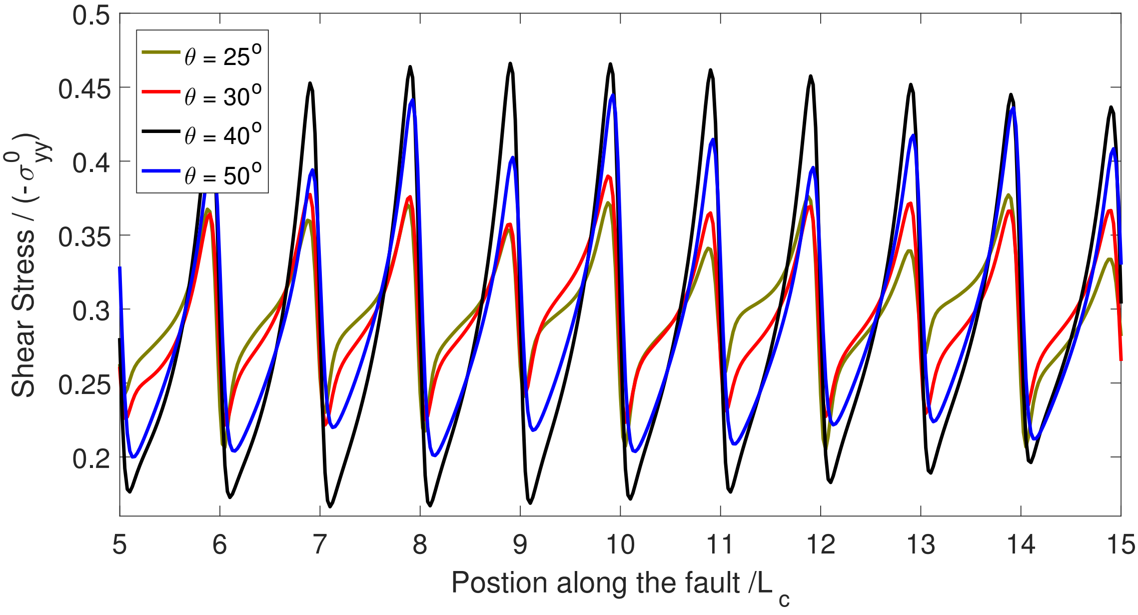

(a)

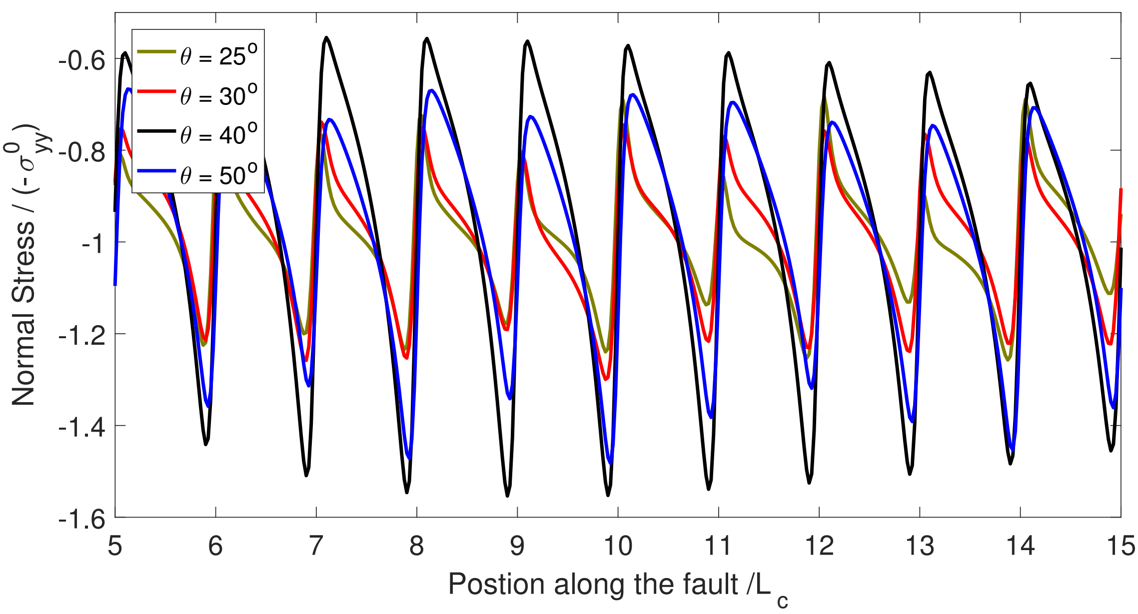

(b)

Figure 14: Shear stress and normal stress distributions on the main fault, at the same point in time, for different orientations of secondary faults with respect to the fault parallel direction $\theta = 25, 30, 40, 50$ degrees in the elastic material case. (a) Shear stress distribution, (b) Normal stress distribution. The amplitude of the stress perturbations decrease as the secondary faults rotate away from the optimally oriented shear plane direction ($\theta = 40$).

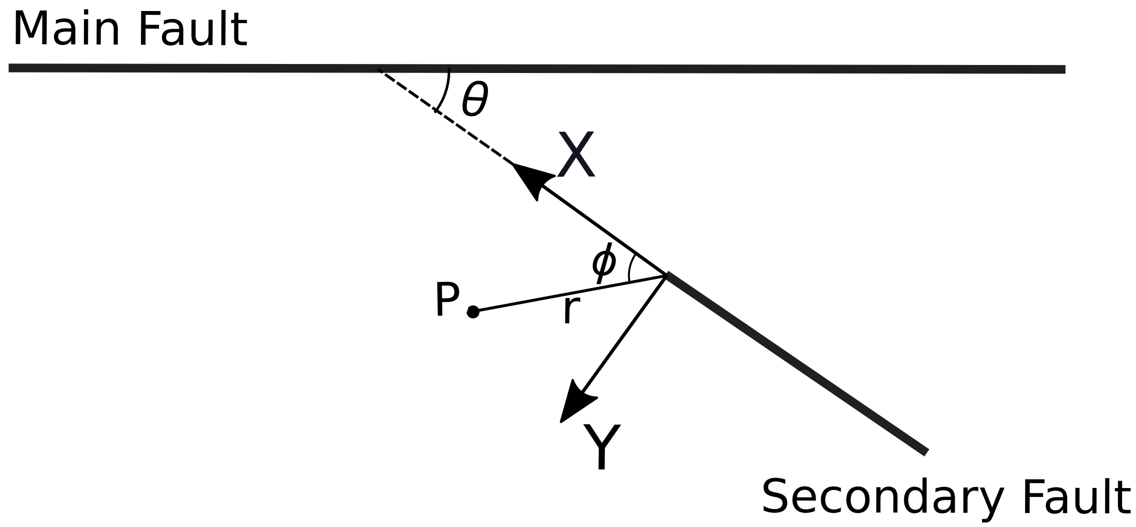

Figure A.1: Model geometry setup for Linear Elastic Fracture Mechanics analysis. The origin of the coordinate system is set at the near end of the secondary fault. The polar coordinates are defined with radius r and angle ϕ. The angle between the main fault and the secondary fault is θ.

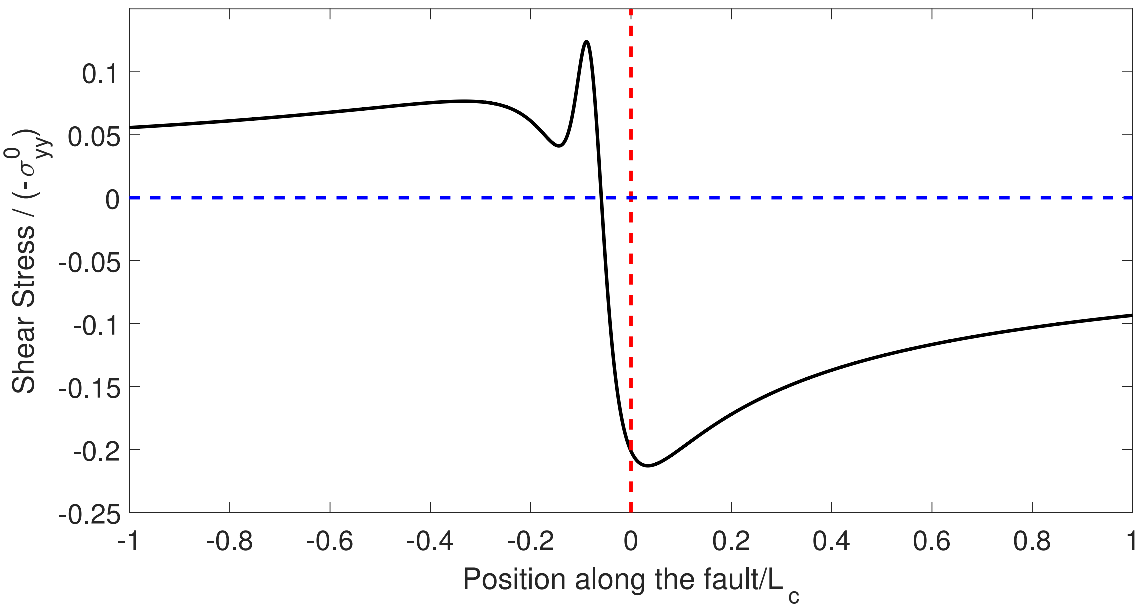

(a)

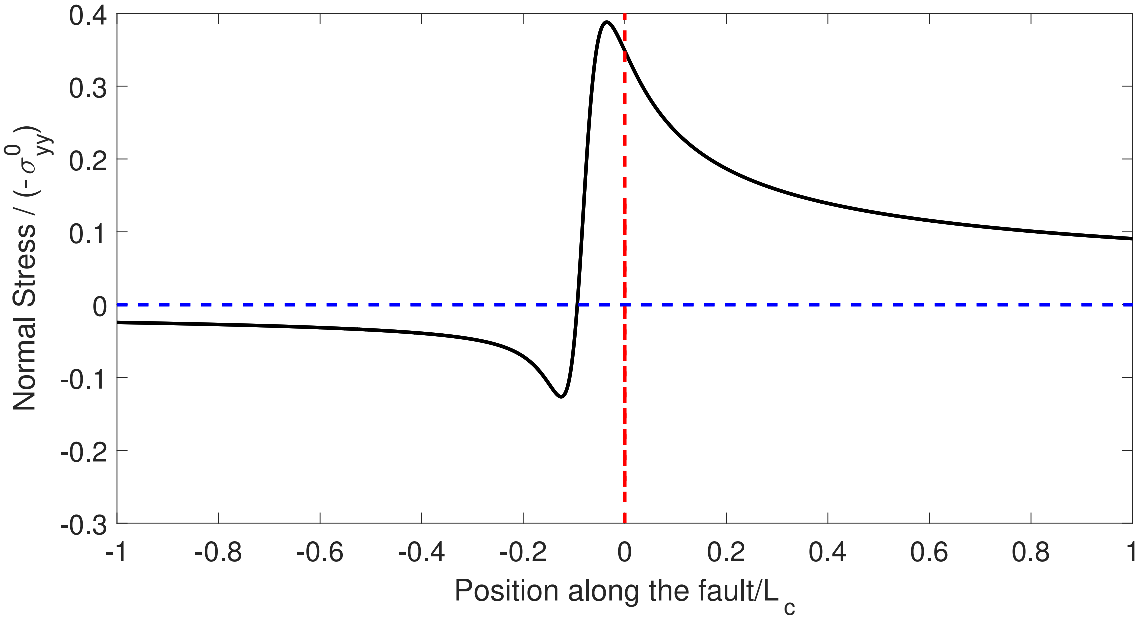

(b)

Figure A.2: Shear and normal stress distribution along the main fault by applying LEFM analysis at the near end of the secondary fault. The secondary fault is located near the position 0 (indicated by the red dash line). The sign of the shear and normal stress switches around the secondary fault position (indicated by the blue dash line). The LEFM analysis gives a stress perturbation pattern that is in qualitative agreement with the results from numerical simulations.